Stony Brook University

Laughlin Quasiparticle Interferometers in the Quantum Hall Regime

A Dissertation Presented

by

Wei Zhou

to

The Graduate School

in Partial Fulfillment of the

Requirements

for the Degree of

Doctor of Philosophy

in

Physics

Stony Brook University

August 2007

Stony Brook University

The Graduate School

Wei Zhou

We, the dissertation committee for the above candidate for the Doctor of Philosophy degree, hereby recommend acceptance of this dissertation.

Vladimir J. Goldman – Dissertation Advisor
Professor, Department of Physics and Astronomy

Peter W. Stephens - Chairperson of Defense
Professor, Department of Physics and Astronomy

Jacobus J. M. Verbaarschot
Professor, Department of Physics and Astronomy

Jiangyong Jia
Assistant Professor, Department of Chemistry

This dissertation is accepted by the Graduate School.

Lawrence Martin
Dean of the Graduate School

Abstract of the Dissertation

Laughlin Quasiparticle Interferometers in the Quantum Hall Regime

by

Wei Zhou

Doctor of Philosophy

in

Physics

Stony Brook University

2007

Laughlin quasiparticles are the low-energy elementary excitations of the fractional quantum Hall condensate. They possess fractional electric charge and obey fractional statistics. The novel Laughlin quasiparticle interferometer devices studied in this dissertation consist of a nearly circular electron island lithographically defined by four etch trenches. The electron island is separated from the 2D electron bulk by two nearly open constrictions. In the quantum Hall regime, chiral edge channels are formed at the periphery of the undepleted 2D electron system. The two counter-propagating chiral edge channels are coupled by tunneling in the constrictions, thus forming an interference path. Two kinds of interferometer devices are studied. For the $e/3$ primary-filling Laughlin quasiparticle interferometer, the constrictions are less depleted, resulting a regime where the whole sample is on the $f = 1/3$ plateau. We obtain the flux period h/e and back-gate charge period $e/3$ for this device. For the second kind of interferometer, the constrictions are more depleted than the first kind device, giving rise to a regime

in which an $f = 2/5$ island is surrounded by $f = 1/3$ fluid. Here we observe superperiodic oscillations with $5h/e$ flux and $2e$ charge periods, both corresponding to excitation of ten island quasiparticles. These periods can be understood as imposed by the anyonic braiding statistics of Laughlin quasiparticles.

To Yingying

Contents

List of Figures viii

List of Tables xiii

Acknowledgements xiv

1 Introduction 1

2 Introduction to quantum Hall effect 3
2.1 Landau levels . . . 3
2.2 Integer quantum Hall effect . . . 4
2.3 Fractional quantum Hall effect . . . 8
2.4 Edge states in the quantum Hall effect . . . 9

3 Samples and measurement techniques 11
3.1 Sample fabrication . . . 11
3.1.1 GaAs/AlGaAs heterojunction . . . 11
3.1.2 Sample fabrication process . . . 12
3.2 Measurement techniques . . . 14

4 Integer quantum Hall regime observations 19
4.1 Aharonov-Bohm quantization condition . . . 19
4.2 Front-gate dependence of the Aharonov-Bohm oscillations . . . 23

5 Detection of fractional statistics of Laughlin quasiparticles 27
5.1 Statistics of Laughlin quasiparticles . . . 27
5.2 $\nu = 1/3$ primary-filling Laughlin quasiparticle interferometer . . . 29
5.3 Aharonov-Bohm superperiod . . . 37

6 Properties of the Aharonov-Bohm superperiod 46
6.1 Flux-period scaling in the Laughlin quasiparticle interferometer 46
6.2 Temperature dependence of the Aharonov-Bohm superperiod . . . 56

7 Conclusion **60**

Bibliography **62**

List of Figures

2.1 A Hall bar sample. The crossed rectangles are Ohmic contacts. 5

2.2 The density of states of a 2DES with disorder. For simplicity, the electron spin is neglected. Each Landau level is broadened due to electrons localized by disorder potentials. However, at the center of each Landau level, there exist extended states. . 6

2.3 Illustration of Laughlin's gedanken experiment. The 2DES is confined on the cylindrical surface. Magnetic field B is pointing from the center out and perpendicular to the surface. A thin flux tube is placed along the axis of the cylinder. By varying the flux inside the flux tube adiabatically, charges are transferred from one end of the cylinder to another. 7

2.4 The energy spectrum for an ideal 2DES of finite size. The boundaries of the 2DES are at y_0 and y_1. n labels each Landau level. At low-temperature, all electron states below the Fermi energy E_F are filled. 10

3.1 A diagram of structure of wafer M97 with the corresponding energy profile showing the conduction band energy E_C, valence band energy E_V, and Fermi energy E_F. Notice the triangular shape potential where the 2DES resides. Wafer structure data are from Ref. [26]. 13

3.2 An illustration of the sample fabrication process. (a) Shaded area is etched to produce the mesa. (b) Four Ohmic contacts are prepared at the corners. (c) Front-gate pattern is defined by electron beam lithography, followed by metal evaporation and lift-off. 15

3.3 A sample mounted on a header. The diagram below shows the names of several parts. Ohmic contacts and front gates are connected to the header pins through gold wires. The thick wire at the bottom right corner connects the backgate to the header pin. Backgate is formed by spreading Indium over a sapphire substrate. 16
3.4 Measurement setup. 18

4.1 An atomic force micrograph of the interferometer sample. Black squares represent Ohmic contacts. Chiral edge channels are coupled in the constrictions by tunneling (shown as dots). . . 20
4.2 Directly measured Aharonov-Bohm oscillation data on the $f = 1$ QH plateau. Regular oscillations are observed for more than 130 periods. The slowly varying background resistance is due to conduction through the bulk and impurity effects. 22
4.3 Aharonov-Bohm resistance oscillations on the f =1, 2, and 4 QH plateaus. A small front-gate voltage is applied to fine tune the symmetry of the tunneling amplitudes, in order to enhance the interference signal. 22
4.4 Aharonov-Bohm oscillation data. Each trace was taken at a fixed front-gate voltage, given in mV in the box close to it. Inset shows a blow-up for the $V_{FG} = 255$ mV trace to show the regularity of the oscillations. 25
4.5 (a) The Aharonov-Bohm Area S_μ as a function of V_{FG}. (b) The dependence of midpoint field of oscillations B_M on V_{FG}. . . . 26

5.1 The interferometer sample. (a) Atomic force micrograph of the island region. (b) Scanning electron micrograph of the island region. Numbered circles represent Ohmic contacts at the four corners of the sample. Chiral edge channels (blue lines) are coupled in the constrictions by tunneling (shown as dots). (c) Illustration of the electron density profile. Note the saddle points in the two constrictions. 30
5.2 Directly measured diagonal R_{XX} and Hall R_{XY} resistance with $V_{FG} = 0$. Constriction fillings are determined from the values of the quantized plateaus. The fine structure is due to quantum interference effects in the residual disorder potential, including the interferometric conductance oscillations as a function of magnetic flux through the island. Inset: the chiral edge channel electron interferometer concept; dots show tunneling. 32

5.3 Representative interference conductance oscillations for electrons, $f = 1$, and for $e/3$ quasiparticles, $f = 1/3$. The magnetic flux period is $\Delta_\Phi = h/e$ in both regimes. Negative front-gate voltage, applied to increase the oscillation amplitude, shifts the oscillations to lower B. 33
5.4 Matched backgate and magnetic field sweep data giving the $e/3$ charge period. (a) The interferometer device is calibrated using the conductance oscillations for electrons, $f = 1$. (b) This calibration gives the charge for the Laughlin quasielectrons $q = 0.33e$. The magnetic flux period $\Delta_\Phi = h/e$, the same in both regimes, implies anyonic statistics of the fractionally charged quasiparticles. 35
5.5 Illustrations of possible fillings for a sample with constrictions. Numbered squares are Ohmic contacts. (a) Both the bulk and the constrictions are on the same quantum Hall plateau. (b) A sample with constriction filling $f_C < f_B$ results in a quantized plateau $R_{XX} = (h/e^2)(1/f_C - 1/f_B)$. (c) The island and the bulk has the same filling f_B, while constriction filling $f_C < f_B$. 39
5.6 Interference of electrons in the integer QH regime. (a),(b) AB oscillations in conductance when one ($f = 1$) or two ($f = 2$) Landau levels are filled. The flux period $\Delta_\Phi = h/e$ gives the outer edge ring radius 685 nm. (c),(d) Positive V_{BG} attracts 2D electrons one by one to the area within the AB path, modulating the conductance. This calibrates the increment $\Delta_{V_{BG}}$ needed to increase the charge by $\Delta_Q = e$. Note that $\Delta_{V_{BG}}$ is independent of f. 40
5.7 Oscillatory conductance for $e/3$ quasiparticles circling an island of $f = 2/5$ FQH fluid. (a) Flux through the island period $\Delta_\Phi = 5h/e$ corresponds to creation of ten $e/5$ quasiparticles in the island [one h/e excites two $e/5$ quasiparticles from the 2/5 FQH condensate, the total (quasiparticles + condensate) charge is fixed]. Such superperiod $\Delta_\Phi > h/e$ has never been reported before. (b) The charge period $\Delta_Q = 2e$ confirms that the $e/3$ quasiparticle consecutive orbits around the 2/5 island are quantized by a condition requiring increment of ten $e/5$ quasiparticles. 41

5.8 (a) Magnetoresistance of the interferometer sample at 10.2 mK. The horizontal arrow shows approximately the $f_C = 1/3$ plateau. Note the *quantized* plateau $R_{XX}(B) = h/2e^2$ at 12.35 T, obtainable only with $f_C = 1/3$, $f_B = 2/5$. (b) The oscillation period ratio for the data of Figures 5.6 and 5.7. $\Delta_B/\Delta_{V_{BG}} \propto 1/f$, independent of the AB path area. The straight line goes through (0, 0) and the $f = 1$ point. Experimental $\Delta_B/\Delta_{V_{BG}}$=21.4 mT/V gives the island filling $f = 2/5$. The crosses (the nearest FQH effect $f = 3/7$ and $1/3$) do not fit the data. 42

6.1 Scanning electron microscope image of the sample. The nearly circular island is defined by four front gates, FG1−FG4. Numbered circles are Ohmic contacts. (a) In the IQH regime, the whole sample is on the same QH plateau. Counterpropagating edge channels (blue lines) are coupled by tunneling (blue dots) in the constrictions. (b) In the FQH regime, an $f = 2/5$ island is enclosed by $f = 1/3$ QH fluid. 48

6.2 (a) A qualitative illustration of the 2D electron density profile. (b) The calculated electron density profile in a circular island defined by an etched annulus of inner radius $R \approx 1050$ nm, $n_B = 1.2 \times 10^{11}$ cm^{-2}. The calculation follows the $B = 0$ model of Ref. [42]. $W = 245$ nm is the depletion length parameter. The blue circles give the radius of the outer edge ring $r_{Out} \approx 685$ nm, obtained from the integer Aharonov-Bohm period and $n(r_{Out})$ from the B-field position on the constriction QH plateaus. The red circles give the inner edge ring radius $r_{In} \approx 570$ nm, obtained with the fractional $N_\Phi = 5$ and the density ratio $n(r_{In})/n(r_{Out}) = (2/5)/(1/3) = 1.20$. 49

6.3 Aharonov-Bohm conductance oscillations δG as a function of B for several values of front gate voltage V_{FG}, given in the labels next to each trace. All the traces are for $f = 1/3$ FQH fluid circling an $f = 2/5$ island, and have been shifted vertically in steps of $0.05e^2/3h$. Each trace contains ∼40 oscillations with a well defined period Δ_B, which depends on V_{FG}. 50

6.4 Dependence of the Aharonov-Bohm period Δ_B on front-gate voltage V_{FG} for (a) $f = 1$ and (b) $f = 2/5$ embedded in $f = 1/3$. The dependence is approximately linear in the range of V_{FG} studied; the solid lines are least squares fits. The $\Delta_B(V_{FG} = 0)$ values give the A-B path areas $S_{Out} = h/e\Delta_B = 1.42 \times 10^{-12}$ m^2 ($f = 1$) and $S_{In} = 5h/e\Delta_B = 0.966 \times 10^{-12}$ m^2 (2/5 embedded in 1/3). 52

6.5 (a) Superperiodic oscillations observed when the $f = 2/5$ island is embedded in the $f = 1/3$ QH fluid. (b) Temperature dependence of the superperiodic oscillations. Each trace was taken at a different temperature from 10.2 mK (bottom trace) to 141 mK (top trace). The successive traces are vertically displaced by 0.4 kΩ. The data in (a) and (b) were obtained on different cooldowns of the sample. 57
6.6 Temperature dependence of the normalized conductance oscillation amplitudes shown on linear and semi-log scale. The spread of data points illustrates the uncertainty. 59

List of Tables

6.1 Summary of results obtained from the experimental Aharonov-Bohm period Δ_B and its dependence on front-gate voltage V_{FG}. Sample M61Dd data is from Ref. [42]. 54

Acknowledgements

I would like to thank many people for helping me finish this dissertation. The text of this dissertation in part is a reprint of the materials as it appears in our previous publications. The co-authors listed in the publications directed and supervised the research that forms the basis for this dissertation.

First of all, I am very much indebted to my advisor Professor Vladimir Goldman for his guidance and financial support. It is through his direct guidance and hand by hand demonstrations that I gradually familiarized myself with the subject we have studied. Beside so much knowledge I learned from him, I also benefited greatly from his attitude of doing research, that is, being careful, well prepared and hard working, which has become an invaluable treasure in my life.

I would like to express my gratitude to Dr. Fernando Camino for many fruitful discussions and warm-hearted helps. Dr. Camino and I joined Professor Goldman's group in the same year. Being an experienced researcher, Dr. Camino taught me to do many tasks in the lab. I also learned a lot about sample fabrication from him. His friendship and help are very important to me.

I would like to thank everybody in the Physics Department for creating such a nice and friendly study environment.

I would like to thank all my friends here for bringing me so much fun. The chattings, dinner parties, and sports with them have created many unforgettable moments, and I of course learned many things from them, too. I thank Jingbin Li, Dan Li, Haijiang Gong, Feng Guo, Jun Guo, Xiaojing Huang, Yaohua Deng, Xin Chen, Haidong Feng, Zhenguo Wang, Xiyue Miao, and Xiaolong Ma for their friendship and many helps.

Finally, I thank my family for their love and support. I deeply thank my wife Yingying Na for her love and care of me during these years I'm abroad. I dedicate this dissertation to her.

Chapter 1

Introduction

Since the discovery of the integer quantum Hall effect (IQHE) in 1980 [1] and the fractional quantum Hall effect (FQHE) in 1982 [2], the field of quantum Hall effect has remained one of the most studied and productive branches of condensed matter physics. The exact quantization of Hall resistance in the IQHE has been established as the new resistance standard and the electron fluid state of the FQHE just brought a new form of matter into reality. The elementary excitations of a fractional quantum Hall (QH) fluid, or Laughlin quasiparticles, possess a fractional electronic charge [3, 4] and obey fractional statistics [5, 6]. These exotic particles have previously existed only in theoretical works [7]. With many accessible condensate states and their intricate internal topological structures [8], the quantum Hall effect provides a unique and excellent test field for such theories and inspires even more. The concept of fault-tolerant topological quantum computation [9] with Laughlin quasiparticles opens a new frontier in QHE research, and may potentially become very useful in applications.

The first unambiguous detection of the fractional charge of Laughlin quasiparticles was done in 1995 [4] in Goldman's group at Stony Brook University, of which the author has been a member for the past four years. The fractional charge of Laughlin quasiparticles is observed in resonant tunneling experiments with quantum antidot devices. An antidot is a small potential hill created by etching a hole in a two dimensional electron system (2DES). However, direct demonstration of fractional statistics of Laughlin quasiparticles has been lacking. The novel Laughlin quasiparticle interferometer samples presented in this dissertation utilize a inverse geometry to that of a quantum antidot device, in which an electron island is separated from the 2D bulk by two wide constrictions. In the quantum Hall regime, counterpropagating edge channels are coupled in the constrictions, thus completing a closed electron orbit around the island. This gives rise to Aharonov-Bohm type interference signals [10] in the

four-terminal sample resistance as a function of the magnetic flux enclosed by the island-circulating electron states located at the chemical potential. Specifically, we observe flux $\Delta_\Phi = 5h/e$ and charge $\Delta_Q = 2e$ periods, in the case a $f = 2/5$ island enclosed by the $f = 1/3$ fluid and flux $\Delta_\Phi = h/e$ and charge $\Delta_Q = e/3$ periods in the case the whole sample is on the $f = 1/3$ QH plateau. To the best of our knowledge, flux period of more than h/e has never been reported before in any Aharonov-Bohm type interference experiments. We attribute the observed Aharonov-Bohm *superperiod* as a direct demonstration of the fractional statistics of Laughlin quasiparticles.

The organization of this dissertation is as the following. In chapter 2, a brief introduction to quantum Hall effect is given. In chapter 3, a detailed description of the sample material and fabrication process is presented, together with an overview of our measurement techniques. Chapter 4 covers our key observations in the integer quantum Hall regime, which provide a solid foundation for the discussions in the following chapters. In chapter 5, we present the main topic of this dissertation, the detection of fractional statistics of Laughlin quasiparticles. Experimental results with two kinds of samples are provided. In chapter 6, properties of the observed Aharonov-Bohm superperiod are investigated, including the front-gate dependence and temperature effects. Finally, chapter 7 concludes the dissertation.

Chapter 2

Introduction to quantum Hall effect

The Laughlin quasiparticle interferometer samples are measured in the quantum Hall regime. This chapter is intended to provide a brief overview of the quantum Hall effect. For more detailed discussions about the issues covered here and beyond, the reader is encouraged to consult books and reviews such as Refs. [11–13]. In Section 2.1, discussions of Landau levels and the roles they play in the quantum Hall effect are provided. In Section 2.2 and 2.3, the experimental observations and basic theories of the integer and fractional quantum Hall effect are covered respectively. Finally, in Section 2.4, the properties of the edge states and their effects on transport measurements are explained.

2.1 Landau levels

For a 2D electron system (2DES) subjected to a perpendicular magnetic field B, the electron states are quantized into discrete energy levels, that is, Landau levels. If we ignore the electron-electron interaction and spin, for a single electron (charge $-e$, and $e > 0$), the Hamiltonian is

$$H = \frac{1}{2m^*}[\mathbf{p} + e\mathbf{A}(\mathbf{r})]^2, \tag{2.1}$$

where m^* is electron effective mass, $\mathbf{p}$ the canonical momentum operator, and $\mathbf{A}(\mathbf{r})$ the vector potential. The quantized Landau levels have energy spectrum

$$E_N = (N + \frac{1}{2})\hbar\omega_c, \tag{2.2}$$

with the cyclotron frequency $\omega_c = eB/m^*$, and N =0, 1, 2, ... The spin of electron causes each Landau level to be split into two levels, which we should refer as spin-polarized Landau levels. The separation of the two spin-polarized Landau levels that belong to the same Landau level is given by the Zeeman energy $\mu_B B$, where μ_B is the Bohr magneton.

The electron state degeneracy for each spin-polarized Landau level is eB/h per unit area. Defining the magnetic length $\ell_0 \equiv \sqrt{\hbar/eB}$, the degeneracy can also be expressed as $1/2\pi\ell_0^2$. The Landau level filling factor ν is defined as

$$\nu \equiv \frac{n}{1/2\pi\ell_0^2} = \frac{nh}{eB}, \tag{2.3}$$

where n is the 2D electron density. The quantization of electron states into Landau levels is essential for the observation of the integer quantum Hall effect, as explained in the next section.

2.2 Integer quantum Hall effect

The integer quantum Hall effect is characterized by the observation of quantized Hall plateaus with values given by the Hall resistance $R_{XY} = V_Y/I_X = h/fe^2$, when the filling factor ν of the 2D electron system is varied. Here f=1, 2, 3, ... is a quantum number, to which we will refer as the exact quantum Hall filling, in contrast to ν, which can be changed continuously. When the Hall resistance is quantized, the diagonal resistance $R_{XX} = V_X/I_X$ will approach zero: the sample is in a dissipationless state. Figure 2.1 shows a diagram about how the measurement is done with a Hall bar pattern. Experimentally, the filling factor can be changed either by changing the 2D electron density via a global backgate, or by changing the magnetic field.

The existence of a quantized Hall plateau is closely related to the broadening of Landau levels due to impurities. In the presence of impurities, the density of states of the 2D electron system can be described as in Figure 2.2. Each Landau level is broadened with tails consisting of localized states. However, at the center of each Landau level, there exist extended states. When the Landau levels are fully filled, the Fermi level is located in the gap between the Landau levels, where there are only localized states. Varying ν only changes the electron distribution within the localized states, which do not carry the transporting current. Thus the Hall resistance is kept constant when the Fermi level resides in the localized states, causing the appearance of the characteristic plateaus.

It should be noted that the quantization of the Hall resistance to h/fe^2

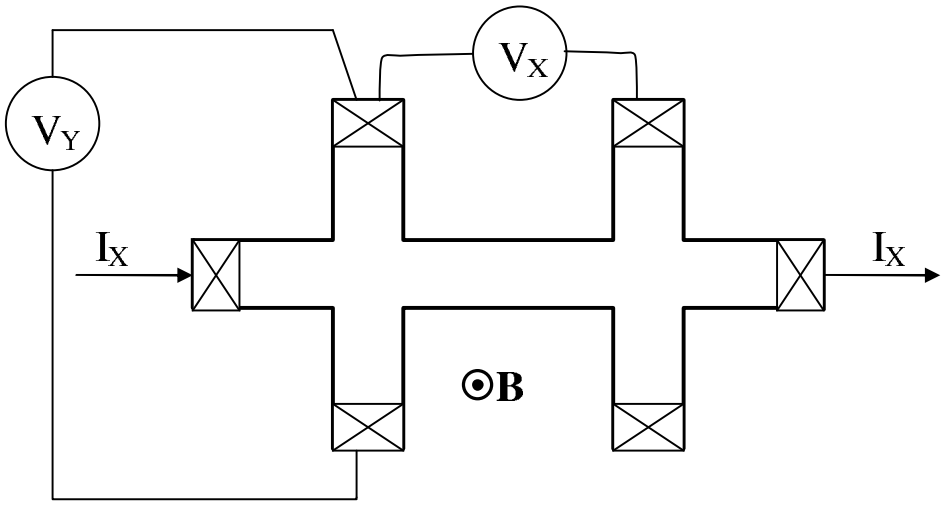

Figure 2.1: A Hall bar sample. The crossed rectangles are Ohmic contacts.

is independent of the sample geometry, material, and contact details. Thus its origin must depend on some fundamental properties of the 2D electron system. Laughlin first provided a general argument based on gauge invariance to explain the exact quantization of the Hall resistance [14]. In his *gedanken* experiment, he considers a 2D electron system on a cylindrical surface, with magnetic field pointing out from the axis and perpendicular to the surface, see Figure 2.3. There is a very thin solenoid placed along the axis (the Y axis). By increasing the flux through the solenoid adiabatically by h/e, the net effect is transferring f electrons from one edge to the other when there are f fully filled Landau levels. This is due to the requirement of gauge invariance of the electron wave function. For the voltage bias V_Y between the two edges, the induced current along the circumference of the cylinder from the flux insertion is $I_X = \partial E/\partial\Phi = \Delta E/\Delta\Phi = eV_Y f/(h/e)$, with E the total energy of the electron system. Thus the Hall resistance $R_{XY} = V_Y/I_X = h/fe^2$.

For the integer quantum Hall effect, the quantum Hall energy gap is provided by the energy separation of two successive Landau levels. The relevant quasiparticles are just electrons and holes. By varying the filling factor, creation of quasiparticles can be achieved by redistribution of electrons to the next empty Landau level or by creating holes in the highest filled Landau level.

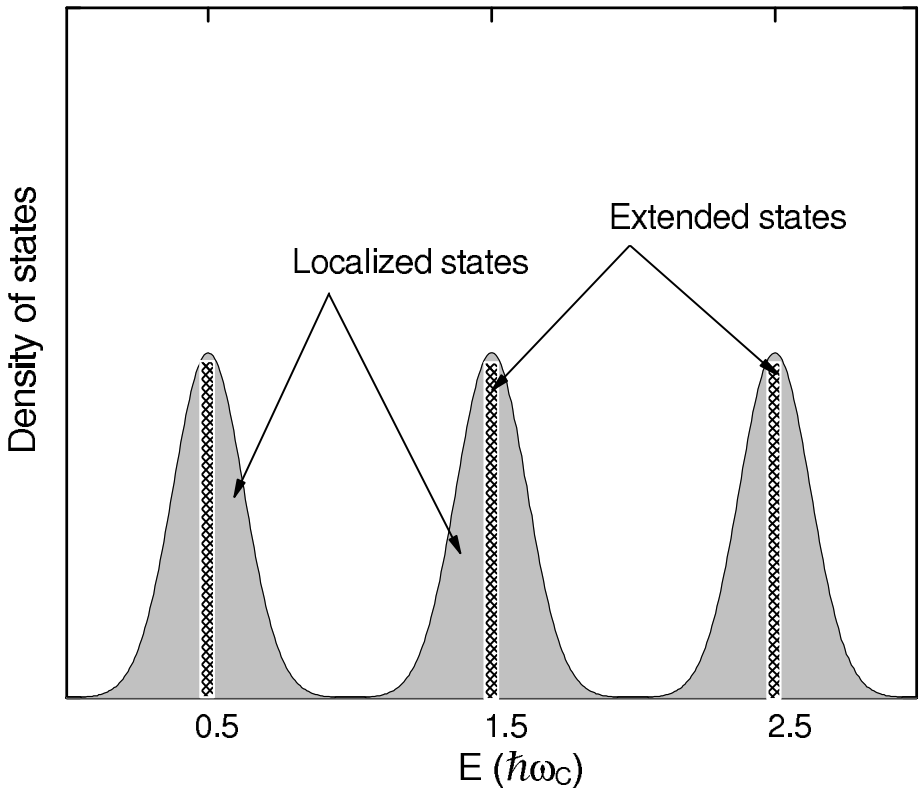

Figure 2.2: The density of states of a 2DES with disorder. For simplicity, the electron spin is neglected. Each Landau level is broadened due to electrons localized by disorder potentials. However, at the center of each Landau level, there exist extended states.

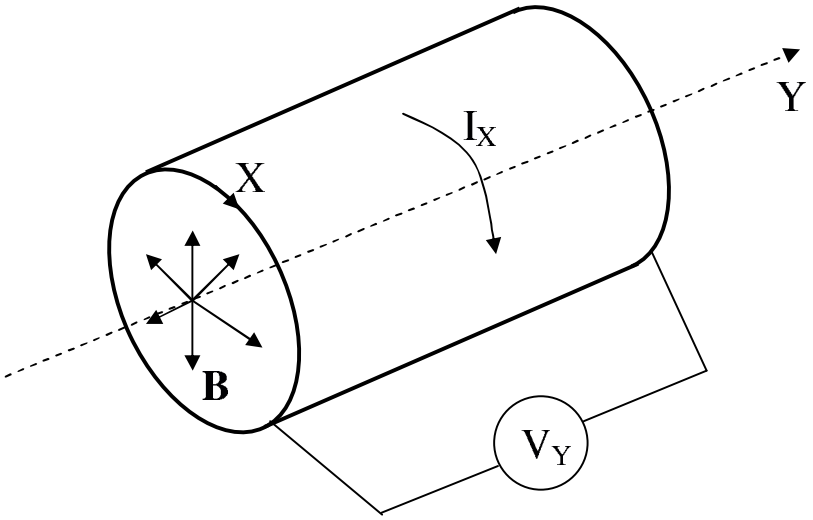

Figure 2.3: Illustration of Laughlin's gedanken experiment. The 2DES is confined on the cylindrical surface. Magnetic field B is pointing from the center out and perpendicular to the surface. A thin flux tube is placed along the axis of the cylinder. By varying the flux inside the flux tube adiabatically, charges are transferred from one end of the cylinder to another.

2.3 Fractional quantum Hall effect

The experimental observation of the fractional quantum Hall (FQH) effect is quite similar to that of the integer quantum Hall effect, such as the quantized Hall plateaus and the concurrent vanishing diagonal resistance. The difference is that the Hall resistance is given by $R_{XY} = h/fe^2$ with f a fractional number. For most of the FQH states, $f = n/m$ with both n and m an integer and m an odd number. However, FQH states with even denominators have also been observed [15, 16]. We shall not discuss the even denominator states since they involve more complex theoretical constructions and are not studied in our experiments.

The existence of quantum Hall effect when only part of the lowest Landau level is occupied suggests the single-particle view used to explain the IQHE may not be applicable here, because the energy gap cannot come from the gap between successive Landau levels. Thus the electron-electron interaction must play an essential role in the FQHE.

Laughlin first proposed a variational wave function [3] for the primary filling FQH sequence $f = 1/m$ with m=3, 5, 7, ... In Laughlin's wave function, the electron-electron correlation effects are taken into account automatically. The wave function has the form

$$\Psi_m = \prod_{j<k} (z_j - z_k)^m \exp\left(-\frac{1}{4\ell_0^2}\sum_l |z_l|^2\right), \tag{2.4}$$

where z_j is the complex coordinate of the electrons on the 2D plane. Numerical simulations show very good overlap between Laughlin's wave function and the true ground state of a 2DES for a few electrons [3, 17]. Laughlin's wave function describes a new form of matter, in which 2D electrons of the partially filled lowest Landau level condense into an electron fluid.

One direct consequence of Eq. 2.4 is the prediction of fractionally charged excitations [3], i.e. quasiparticles, from the electron condensate. For the filling $f = 1/m$, the quasielectrons and quasiholes have charge $q = -e/m$ and $q = e/m$, respectively. When the filling factor is not equal to the exact filling, $\nu \neq f$, the ground state of the 2DES consists of the exact filling condensate and the matching density of quasiparticles.

Based on the fundamental work of Laughlin, Haldane [18] and Halperin [6] proposed a hierarchical construction for the general fillings $f = n/m$. The basic idea is that the quasiparticles of one *parent* condensate condense into a new fractional quantum Hall state, forming a *daughter* state. By applying this process repeatedly, all possible fractions can be obtained. It is also found that for the general filling $f = n/m$, the relevant quasiparticles possess charge

$\pm e/m$ [18]. In addition to fractional charge, Laughlin quasiparticles obey fractional statistics, which we will explore in detail in Chapter 5.

2.4 Edge states in the quantum Hall effect

For a 2DES subjected to perpendicular magnetic field B, the electron states near the edge of the 2DES are particularly important in transport measurements. The confining potential raises the energy of states near the edge and results in quasi-one-dimensional extended states along the edge, that is, the edge states [19, 20]. It has also been shown that the edge states can survive moderate disorder [19]. On a quantized Hall plateau, the current is carried only by edge states, since in the bulk there are only localized states near the Fermi level.

In the integer quantum Hall regime, for each filled bulk spin-polarized Landau level, there are corresponding edge states of that level near the edge, with energy above the bulk state, see Figure 2.4. All edge states belonging to the same edge carry current in the same direction, determined by the perpendicular magnetic field B and the confining potential. Edge states belonging to a given Landau level are also referred as edge channels, and typically represented as lines with arrows in a diagram. If the chemical potential differs by Δ_μ between counterpropagating edge channels of a sample, the net current carried by them is [19]

$$I_X = fe\Delta_\mu/h, \tag{2.5}$$

with f the number of filled Landau levels. Since $\Delta_\mu = eV_Y$, we obtain the quantized Hall resistance $R_{XY} = h/fe^2$.

In the fractional quantum Hall regime, the description of edge states is more complicated, due to the importance of electron-electron interaction. The edge channels are usually modeled as a one dimensional chiral Luttinger liquid (χLL) [8, 20]. The low-energy charged excitations, or Laughlin quasiparticles, of such χLL are gapless [8], unlike the case in the bulk condensate, and carry the transport current in the fractional quantum Hall regime.

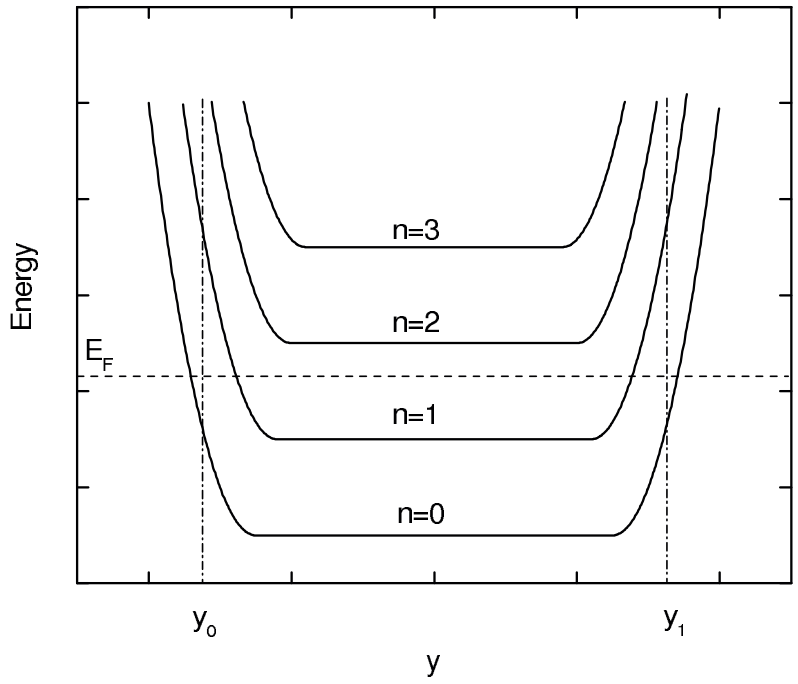

Figure 2.4: The energy spectrum for an ideal 2DES of finite size. The boundaries of the 2DES are at y_0 and y_1. n labels each Landau level. At low-temperature, all electron states below the Fermi energy E_F are filled.

Chapter 3

Samples and measurement techniques

The novel Laughlin quasiparticle interferometer devices described here are based on low disorder, high mobility GaAs/AlGaAs heterojunctions. The fabrication process includes several steps, such as optical lithography, electron lithography and metal evaporation. The sample is cooled in a dilution refrigerator and four-terminal resistance is measured with a lock-in phase technique. In Section 3.1, a description of the sample material and fabrication process is presented. In Section 3.2, the low-temperature equipment and measuring techniques will be introduced.

3.1 Sample fabrication

3.1.1 GaAs/AlGaAs heterojunction

Our samples are fabricated from high-quality GaAs/AlGaAs heterojunctions grown by Molecular Beam Epitaxy (MBE) [21]. It is well known that GaAs is a single-valley, direct gap, isotropic insulator. Substituting a fraction ($\leq 40\%$) of the Ga atoms by Al, the resulting $Al_xGa_{1-x}As$ still has similar properties as GaAs, except a larger band gap [22]. MBE allows to grow layers of $Al_xGa_{1-x}As$ on top of the GaAs substrate with atomically sharp interface. If $Al_xGa_{1-x}As$ is doped with donors, which typically are Si, electrons from the donors can be excited thermally or by exposing to light and move across the interface. The resulting potential at the interface has a triangular shape, see Figure 3.1. The electron states in the triangular potential are quantized, forming different subbands [23]. For a typical doping of $Al_xGa_{1-x}As$ with x=0.3 and donor concentration of order 10^{11} cm^{-2}, only the lowest subband is occupied at low

temperature, effectively resulting a 2D electron system. However, it should be noted that the electron wave function in the lowest subband still has some extent in the direction perpendicular to the 2D plane, which is about several magnetic lengths $\ell_0 = \sqrt{\hbar/eB}$, with B the magnetic field.

Several factors account for the high mobility of the 2D electron system realized in GaAs/AlGaAs heterojunction, which is crucial for experiments of fractional quantum Hall effects. First, the spatial separation of donors from the 2D electrons reduces electron scattering from ionized donors. Second, the atomically sharp interface causes less scattering due to interface roughness. Third, the similarity of dielectric constants of GaAs and AlGaAs creates less image potential, which also reduces electron scattering. In addition, the small effective electron mass $m^* \approx 0.065m_e$, with m_e the electron mass, gives rise to a larger cyclotron frequency $\omega_c = eB/m^*$, which results in a larger separation of Landau levels and facilitates the appearance of quantum Hall effect.

The heterojunction material used to fabricate the interferometer sample is grown by the Varian Gen II MBE system at Princeton University [24–26]. A diagram of the heterojunction for wafer M97 is provided in Figure 3.1. Other heterojunctions used for sample fabrication also have similar structures as shown here.

3.1.2 Sample fabrication process

Here we present a typical sample fabrication process. Depending on the design, the parameters used in a real sample may differ from the values here.

The sample is roughly a 4×4 mm square cut from the GaAs/AlGaAs wafer. After 4-cycle cleaning, which is done by rinsing the sample with TCE, Acetone, Methanol, and de-ionized (DI) water in ultrasonic bath each for 1 min successively, in the specified order. The sample is mounted on a glass slide, and, subsequently, a thin layer of 1813 photo resist is spinned at 4000 rpm for 30 sec. The sample is baked at 95 °C for 30 min. Then it is covered by an optical mask of the mesa pattern and exposed to ultraviolet light for 30 min. After exposure, the photo resist is developed in 352 developer for 45 sec. The sample is subsequently etched in 1 H_2SO_4:8 H_2O_2:100 H_2O at 1.5 °C for the desired depth. After etching, the remaining photo resist is removed in acetone. This completes the mesa definition.

Next, four Ohmic contacts at each corner of the sample are prepared by alloying with In metal at 410 °C in Hydrogen atmosphere for 7 min. Then the sample is gradually cooled to room temperature.

Then the sample is cleaned by 4-cycle cleaning and glued to a macor holder. A thin layer photo resist of 4% PMMA is spinned at 5000 rpm for 45 sec and subsequently baked at 170 °C for 30 min. The front gate patterns are defined

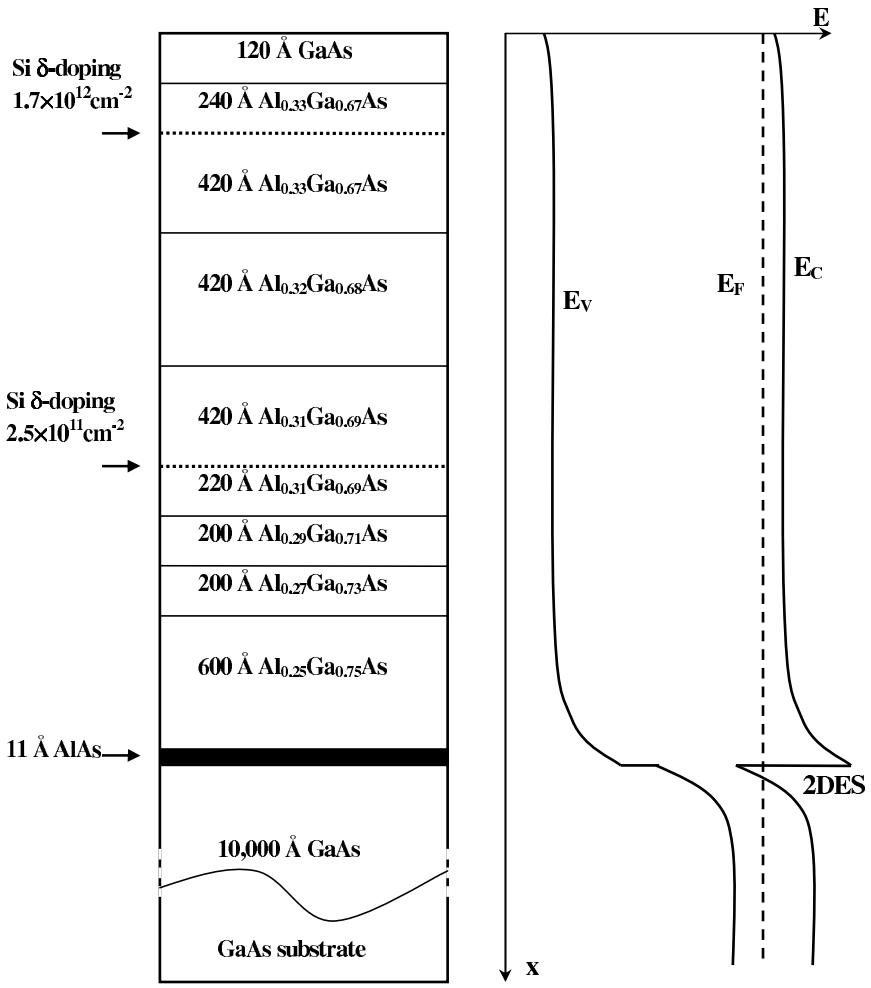

Figure 3.1: A diagram of structure of wafer M97 with the corresponding energy profile showing the conduction band energy E_C, valence band energy E_V, and Fermi energy E_F. Notice the triangular shape potential where the 2DES resides. Wafer structure data are from Ref. [26].

by electron-beam lithography. After exposure to electron beam, the PMMA is developed in 1 MIBK:3 IPA at 21 °C for 55 sec. The developed sample is baked at 95 °C for another 30 min and then etched to the desired depth in 1 H_2SO_4:8 H_2O_2:100 H_2O at 1.5 °C.

The sample, with the remaining photo resist still on top, is brought to the BOC Edwards Auto 306 metal deposition system. A 5 nm Ti layer followed by 45 nm Au is deposited on top of the sample. Then the sample is placed in acetone for lift-off. Only the metal deposited in the etched front gate area will remain, the rest just comes off with the photo resist. Figure 3.2 shows a summary of the above processes.

The next step is to prepare a backgate for the sample. First, a chip of single crystal sapphire is cut with slightly larger size than the sample. Then the sapphire chip is covered with a thin layer of In metal and placed on top of a hot plate, in order to keep the Indium molten. The sample is placed on top of the sapphire chip, with Indium in between. The Indium layer now forms the global backgate of the sample.

In order to perform transport measurement, the sample must first be mounted to a header, which is a chip holder with pins that can be plugged into the sample probe. The Ohmic contacts, the front gates, and the backgate contacts are all connected to the header pins by gold wires, see Figure 3.3.

3.2 Measurement techniques

We use an Oxford Instrument TLM-400 top-loading-into-mixture ^{3}He-^{4}He dilution refrigerator to provide the ultralow temperature. The base temperature of the system is 10.2 mK. Temperature is measured with a Dale 750 Ω resistor, which is placed close to the sample and calibrated with ^{60}Co nuclear orientation absolute thermometry for T$\leq$ 40 mK and against a commercially calibrated resistor for T$\geq$ 25 mK. The refrigerator has a built-in Nb_3Sn superconducting magnet that produces nearly uniform magnetic field at the position where the sample is located, where the homogeneity is around 7.7 parts in 10^4 over a distance of 10 mm. At liquid He temperature (4.2 K), the magnet can provide up to 14 T magnetic field. By turning on the λ-plate refrigerator attached to the magnet, a high-field of 17 T is obtainable. The magnet is powered with an IPS-120 power supply, which can be operated with ramp current or persistent current mode, and easily controlled by a computer program. The magnetic field is calculated from the current through the magnet measured with an HP 3458A multimeter.

A diagram of the measurement setup is shown in Figure 3.4. The header (with sample mounted) is plugged into the sample probe and inserted into

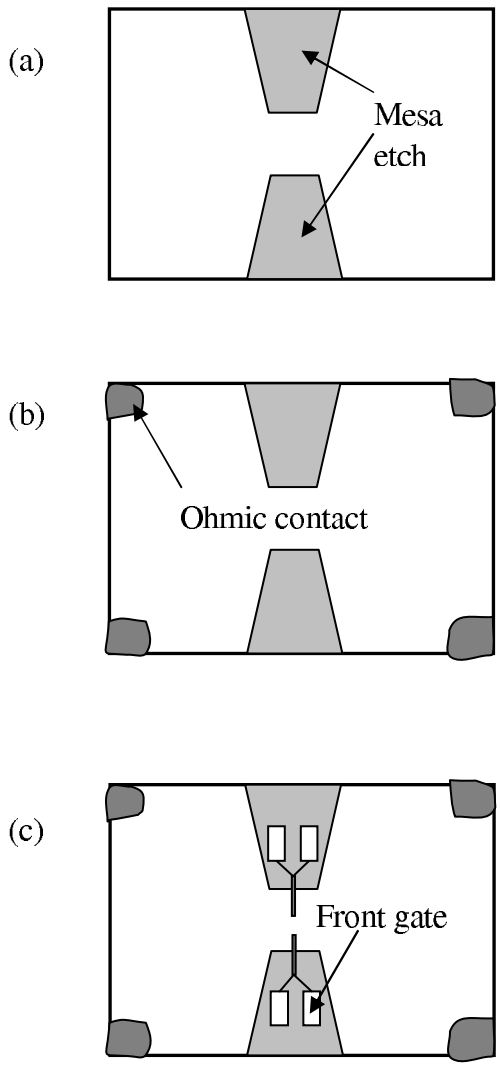

Figure 3.2: An illustration of the sample fabrication process. (a) Shaded area is etched to produce the mesa. (b) Four Ohmic contacts are prepared at the corners. (c) Front-gate pattern is defined by electron beam lithography, followed by metal evaporation and lift-off.

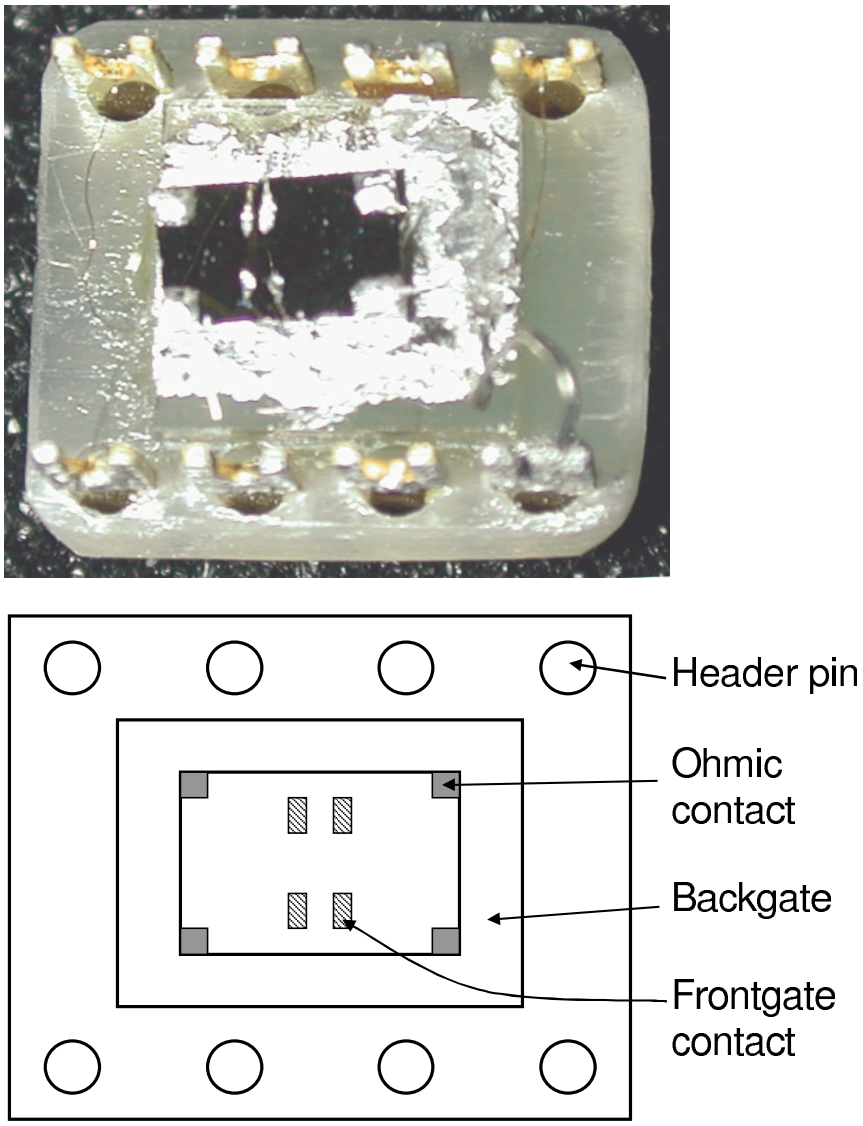

Figure 3.3: A sample mounted on a header. The diagram below shows the names of several parts. Ohmic contacts and front gates are connected to the header pins through gold wires. The thick wire at the bottom right corner connects the backgate to the header pin. Backgate is formed by spreading Indium over a sapphire substrate.

the tail of the mixing chamber, which is located at the center of the magnet. The excitation current is from the oscillator output of the EG&G model 5302 lock-in amplifier. The resulting signal from the sample is detected by the same lock-in amplifier. Extensive cold filtering is used to reduce the electromagnetic noise incident on the sample. The sample temperature is monitored by another EG&G model 5301 lock-in amplifier that measures the temperature sensor (Dale 750 Ω resistor) located close to the sample, see Figure 3.4.

The four-terminal sample resistance is measured as a function of the magnetic field or the backgate voltage. The four independently contacted front gates are used primarily to fine-tune the symmetry of constrictions. The backgate voltage can be ramped up or down continuously in the range about −10 V to +10 V with good precision by a ramp generator. The front gates are connected to a high precision, high stability voltage source powered by batteries, whose output voltage is measured with a digital multimeter.

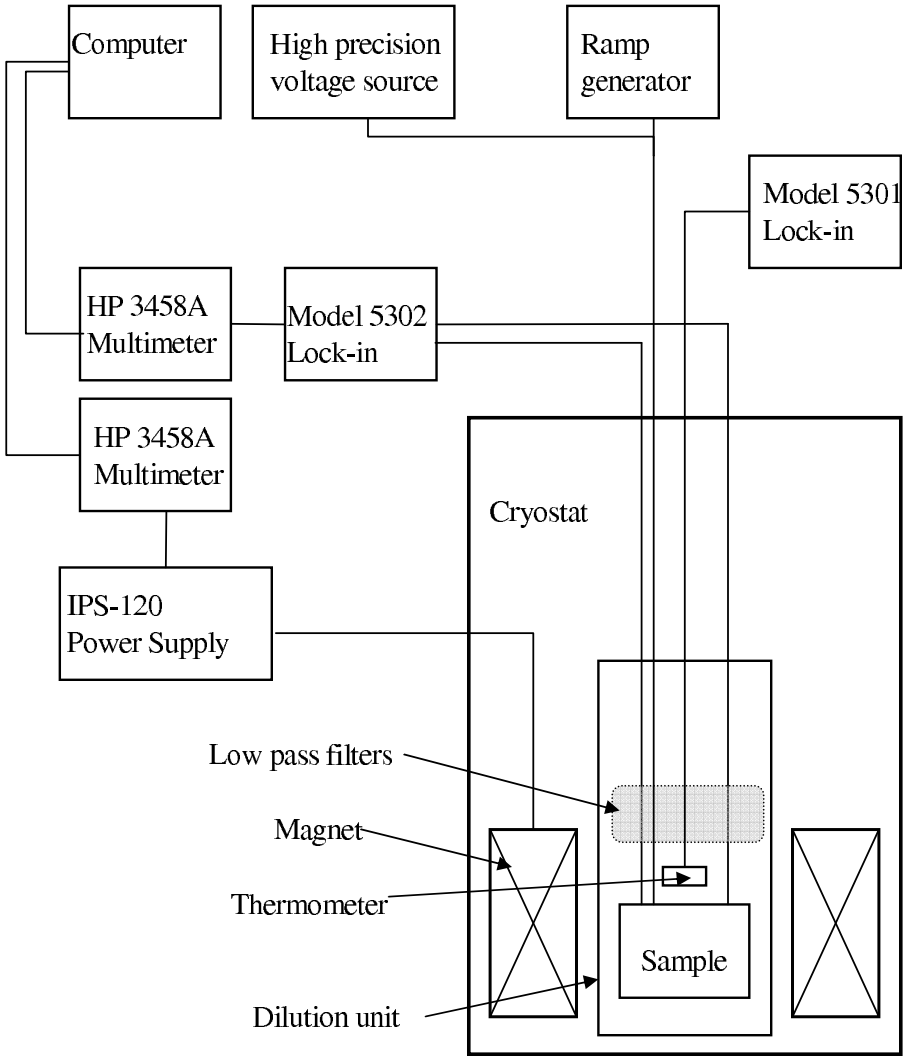

Figure 3.4: Measurement setup.

Chapter 4

Integer quantum Hall regime observations

An interferometer device is shown in Figure 4.1. A nearly circular electron island is defined by four etch trenches with front-gate metal deposited in. The island is separated from the 2D electron bulk by two nearly open constrictions. In the IQH regime the whole sample may stay on the same QH plateau. Two counterpropagating edge channels are coupled by tunneling in the constrictions, thus forming a closed electron interference path. In Section 4.1 we present Aharonov-Bohm oscillation data on several integer quantum Hall plateaus. The magnetic field periods Δ_B agree very well with that given by the Aharonov-Bohm quantization condition, which requires the quantized electron orbitals enclosing flux of integer multiple of h/e. In Section 4.2, the front-gate bias dependence of the Aharonov-Bohm oscillations is discussed. We find a systematic shift to high-B of the oscillation region and simultaneously decreasing magnetic field period Δ_B as the front-gate voltage is increased.

4.1 Aharonov-Bohm quantization condition[1]

Quantum interference in the QH regime of 2D electrons around a quantum antidot, which is a potential hill defined by etching a hole in a 2DES, has been used experimentally to determine the fractional charge of Laughlin quasiparticles of the surrounding quantum Hall condensate [4, 30]. Our current devices utilize the inverse geometry. The layout resembles qualitatively a "coulomb island" [31, 32], but the constrictions are nearly open, so that no Coulomb

[1]Part of this section published in Wei Zhou, F. E. Camino, and V. J. Goldman, proceedings of LT24, AIP Conference Proceedings Vol. **850**, 1351 (2006), F. E. Camino, W. Zhou, and V. J. Goldman, Phys. Rev. B **72**, 155313 (2005).

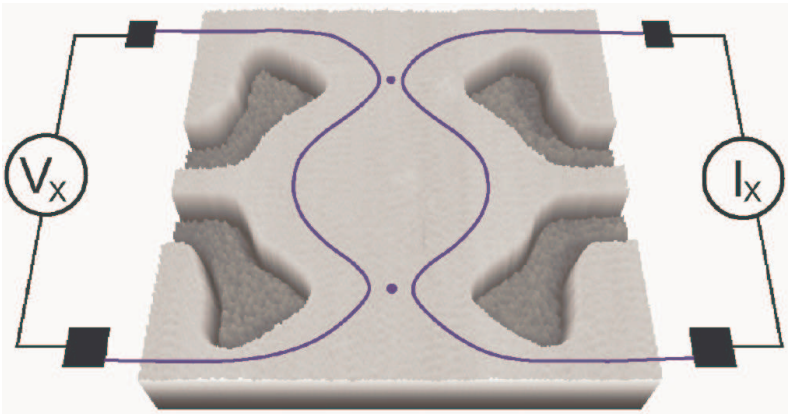

Figure 4.1: An atomic force micrograph of the interferometer sample. Black squares represent Ohmic contacts. Chiral edge channels are coupled in the constrictions by tunneling (shown as dots).

blockade or conductance steps are observed.

On a QH plateau, when tunneling between the constriction edge channels occurs, in the quantum-coherent regime, Aharonov-Bohm oscillations with period Δ_B are expected in the four-terminal resistance $R_{XX} = V_X/I_X$ as a function of the magnetic field B. In the quantum limit, each oscillation signals the alignment of a quantized electron state encircling the 2D electron island with the chemical potential μ.

In each spin-polarized Landau level, the single-electron states are quantized by the Aharonov-Bohm condition: The magnetic flux Φ through the area of an encircling orbital S_m satisfies $\Phi = BS_m = m\Phi_0$, where m is the quantum number of the orbital and $\Phi_0 = h/e$ is the fundamental flux quantum [35]. Thus, $S_m = mh/eB = 2\pi m\ell_0^2$, where $\ell_0 = \sqrt{\hbar/eB}$ is the magnetic length, and the area for each electron state per spin-polarized Landau level is $S_{m+1} - S_m = 2\pi\ell_0^2 = h/eB$. These quantization conditions apply as well to an interacting 2D electron fluid with microscopically uniform density, so long as no phase transition to a charge density wave (such as a striped or "bubble") ground state occurs.

The interferometer samples were fabricated from a low disorder, high mobility GaAs/AlGaAs heterojunction material where 2D electrons (285 nm below the surface) were prepared by exposure to red light at 4.2 K. The electron island of lithographic radius $R \approx$1050 nm was defined by four etch trenches of etch depth 140 nm. Au/Ti metal was deposited into the etch trenches by a self-aligned lift-off process to form the front gates, see Figure 4.1. For the 2D bulk density $n_B = 1.2 \times 10^{11}$ cm^{-2}, there are $\sim$2000 electrons in the island.

Samples were cooled to 10.2 mK in the ^{3}He-^{4}He mixture inside the mixing chamber of a dilution refrigerator. Four-terminal resistance $R_{XX} = V_X/I_X$ was measured by passing a 100 pA, 5.4 Hz ac current through two contacts, and detecting the voltage between the other two contacts by a lock-in-phase technique. Extensive cold filtering cuts the integrated electromagnetic "noise" environment incident on the sample to $\sim 5 \times 10^{-17}$ W, which allows us to achieve a low electron temperature of 18 mK in a mesoscopic sample [28].

We observe Aharonov-Bohm type oscillations in the four-terminal resistance R_{XX} on the IQH plateaus. Figure 4.2 presents a typical directly measured R_{XX} vs. B trace with about 130 well-defined oscillation periods. The oscillations are clearly periodic with period Δ_B. For example, the trace shown in Figure 4.2 ($V_{FG} = 232$ mV) has $\Delta_B = 2.62$ mT, which yields an interference area $S_\mu = h/e\Delta_B = 1.58 \times 10^{-12}$ m^2 according to the Aharonov-Bohm quantization condition. Figure 4.3 shows the measured Aharonov-Bohm oscillations on the f =1, 2, and 4 plateaus. For clarity, a smooth background onto which the oscillations are superimposed is subtracted from the directly measured data. The small differences in the front-gate voltages for different fillings in Figure 4.3 are for fine-tuning the tunneling amplitude symmetries in the two constrictions, in order to enhance the oscillation amplitude. For $f = 1$, the magnetic field period Δ_B=2.81 mT, resulting an Aharonov-Bohm area $S_\mu = h/e\Delta_B = 1.47 \times 10^{-12}$ m^2. For $f = 2$, there are two filled spin-polarized Landau levels. Thus two oscillations per h/e are expected. Indeed, we find $\Delta_B = 1.43$ mT for $f = 2$, this gives the Aharonov-Bohm area $S_\mu = h/2e\Delta_B = 1.45 \times 10^{-12}$ m^2. Similarly, we obtain $S_\mu = 1.54 \times 10^{-12}$ m^2 with $\Delta_B = 0.67$ mT for $f = 4$. Within our experimental accuracy, the Aharonov-Bohm areas are constant for all three fillings, independent of B.

It should also be noted that changing B does not change appreciably the number of electrons within S_μ. Otherwise, huge Coulomb charging energy would be incurred. For example, if each of the 100 observed oscillations on the $f = 1$ plateau is resulted from transferring of one electron into S_μ, the total charging of $100e$ of the island would result in $\sim$10 eV charging energy, which is much higher than the experimental energy scale. Instead, changing B changes the density of states in each Landau level, so that the same number of island electrons occupies the same total number of states, but their distribution between various Landau levels changes: The Landau level filling $\nu = nh/eB$ changes while density n is fixed. The chemical potential in the island is determined by the μ in the bulk. The data in Figure 4.3 show that apparently the radial position of the edge channels circling the island is nearly fixed by the confining potential, that is, S_μ is nearly constant. The quantum number m_μ of the state S_m corresponding to S_μ regularly changes in steps of one, $m_\mu \propto B$

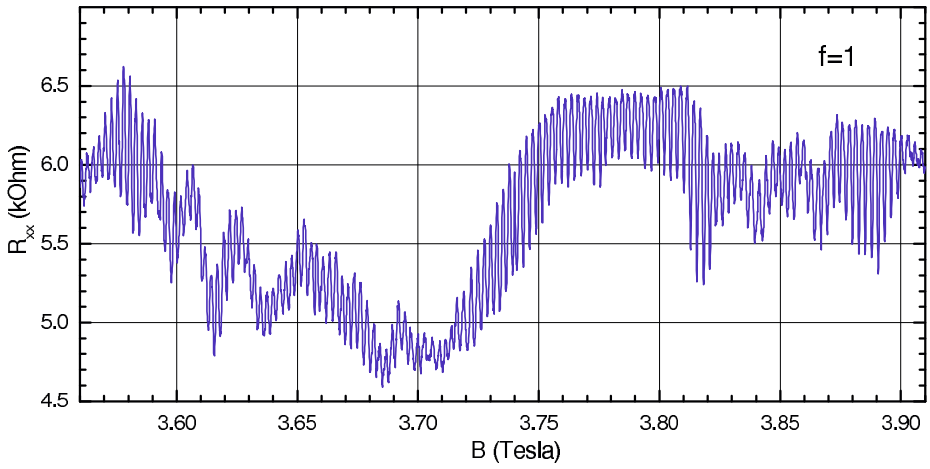

Figure 4.2: Directly measured Aharonov-Bohm oscillation data on the $f = 1$ QH plateau. Regular oscillations are observed for more than 130 periods. The slowly varying background resistance is due to conduction through the bulk and impurity effects.

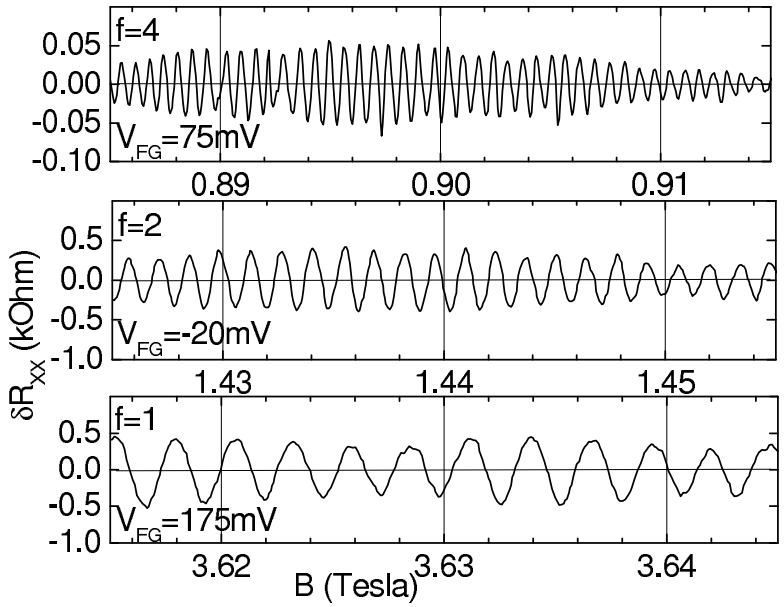

Figure 4.3: Aharonov-Bohm resistance oscillations on the f =1, 2, and 4 QH plateaus. A small front-gate voltage is applied to fine tune the symmetry of the tunneling amplitudes, in order to enhance the interference signal.

since the area per state $2\pi\ell_0^2 \propto 1/B$. If the occupation of the states in the electron island were a step-function, 1 for $m \leq m_\mu$ and 0 for $m > m_\mu$, then S_μ must change, and the number of electrons within S_μ must change. Instead, as evidenced by the above data, both S_μ and the number of electrons within S_μ are nearly constant. What happens is that the electron occupation is not described by the step-function. Increasing B increases density of states in a Landau level, thus accommodating the same number of electrons is accompanied by creation of unoccupied states (that is, holes) in the otherwise filled Landau level. Likewise, decreasing B is accompanied by filling of the states in the next, otherwise empty Landau level. Such Landau level quasiparticle or quasihole creation allows to accommodate a fixed number of island electrons (as dictated by the selfconsistent electrostatics of Coulomb-interacting electrons) in a nearly constant area S_μ.

In summary, we observe Aharonov-Bohm oscillations on the f =1, 2, and 4 QH plateaus. The results show that the interference area is nearly independent of B. This is in good agreement with the Aharonov-Bohm quantization condition, without any significant modification due to the confining potential.

4.2 Front-gate dependence of the Aharonov-Bohm oscillations[2]

The main confining potential for the island electrons is produced by the etch trenches which remove the donors. GaAs is known to have the "surface Fermi level pinning," due to a large density of mid-gap surface electron states, which has been successfully modeled by self-consistent depletion of donors, including a negative surface charge density [56]. The surface depletion results in the 2D electron density being less than the donor density (because some donor electrons go to the surface), and, important for the present samples, an additional etched mesa sidewall depletion due to the free surface of the etch trenches. The front gates are formed by Au/Ti metal deposited into the etch trenches. Application of a front-gate voltage V_{FG} produces electric field which affects the confining potential and thus changes both the electron density distribution and S_μ, which is the interference path area. The number of electrons in the island changes because both density and the area S_μ change. An increased n is accompanied by the shift to a higher B of the QH plateau onto which the Aharonov-Bohm oscillations are superimposed. An increase of S_μ is observed as a smaller Aharonov-Bohm period Δ_B. Thus the two effects are measured

[2]Part of this section published in F. E. Camino, W. Zhou, and V. J. Goldman, Phys. Rev. B **72**, 155313 (2005).

directly, independent of each other.

The sample M61Dd studied here is based on a high quality GaAs/AlGaAs heterojunction, which has 2D bulk electron density $n_B = 9.7 \times 10^{10}$ cm^2 after exposing to red light at 4.2 K. The island of lithographic radius $R \approx 1300$ nm was defined by four etch trenches with electron-beam lithography. After a 82 nm etching, 50 nm thick Au/Ti gate metal was deposited into the etch trenches. The sample was cooled to 10.2 mK in the dilution refrigerator. Four-terminal resistance $R_{XX} = V_X/I_X$ was measured by passing ac current through the sample and detecting the resulting signal with a lock-in-phase technique. We typically apply $I_X = 200$ pA rms ac current, although reducing $I_X = 100$ pA reveals moderate electron heating effects.

For this sample we will focus on the $f = 1$ QH plateau only. We observe the Aharonov-Bohm oscillations in R_{XX}, superimposed on a smooth background magnetoresistance. Figure 4.4 presents the oscillatory δR_{XX} as a function of B for several positive V_{FG}. δR_{XX} is obtained by subtracting the smooth background from R_{XX}. The period Δ_B for each of these traces decreases with increasing V_{FG}. Thus S_μ increases with increasing V_{FG}. We find an approximately linear relationship between S_μ and V_{FG}, with slope $dS_\mu/dV_{FG} = 1.44 \times 10^{-12}$ m^2/V, see Figure 4.5(a). It is evident that the magnetic field intervals where the Aharonov-Bohm oscillations occur shift to higher B as V_{FG} is increased. To quantify this behavior, we define B_M as the midpoint of the magnetic field range in which the oscillations occur for a specific V_{FG}. For example, $B_M \approx 2.80$ T for the $V_{FG} = 150$ mV trace. Figure 4.5(b) shows the dependence of thus determined B_M on V_{FG}, which is approximately linear in the range of the voltages studied, with slope $dB_M/dV_{FG} = 1.77$ T/V. Assuming $\nu = 1$ occurs at B_M, this corresponds to the $f = 1$ edge channel density $n(r_\mu) = eB_M/h$ to vary with V_{FG} as $dn(r_\mu)/dV_{FG} = 4.3 \times 10^{14}$ 1/m^{2}V.

In conclusion, on the $f = 1$ quantum Hall plateau, we observe a systematic shift to high-B of the oscillation region and the concurrent decrease of magnetic field period Δ_B as the front-gate voltage V_{FG} is increased. We also find an approximately linear relation of the oscillation midpoint field B_M and the interference area S_μ as a function of V_{FG}. Later in Section 6.1 we will further discuss the front-gate effects in the fractional quantum Hall regime.

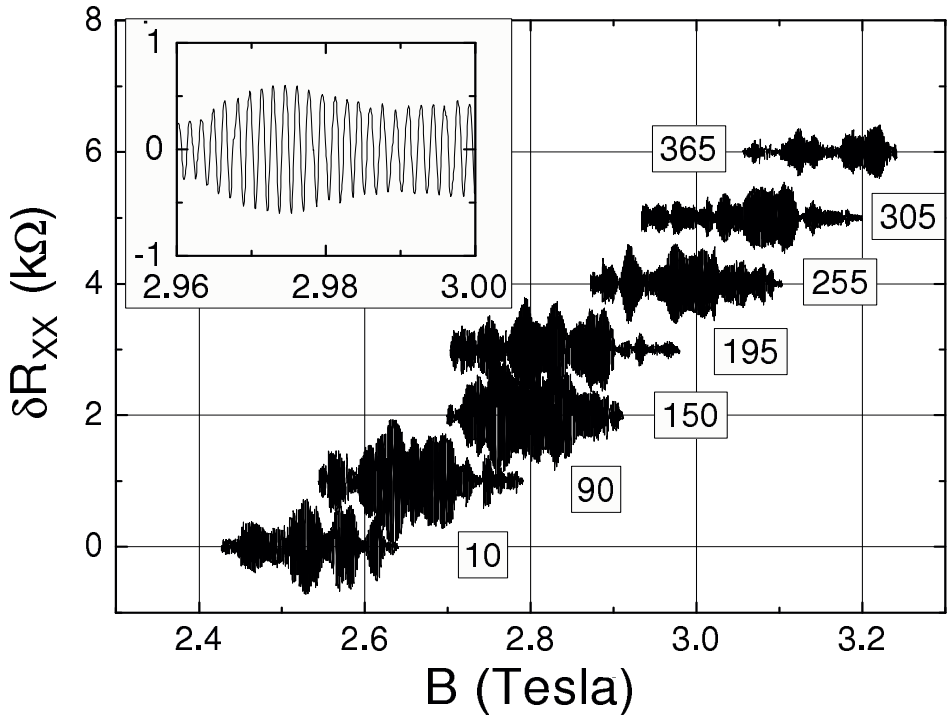

Figure 4.4: Aharonov-Bohm oscillation data. Each trace was taken at a fixed front-gate voltage, given in mV in the box close to it. Inset shows a blow-up for the $V_{FG} = 255$ mV trace to show the regularity of the oscillations.

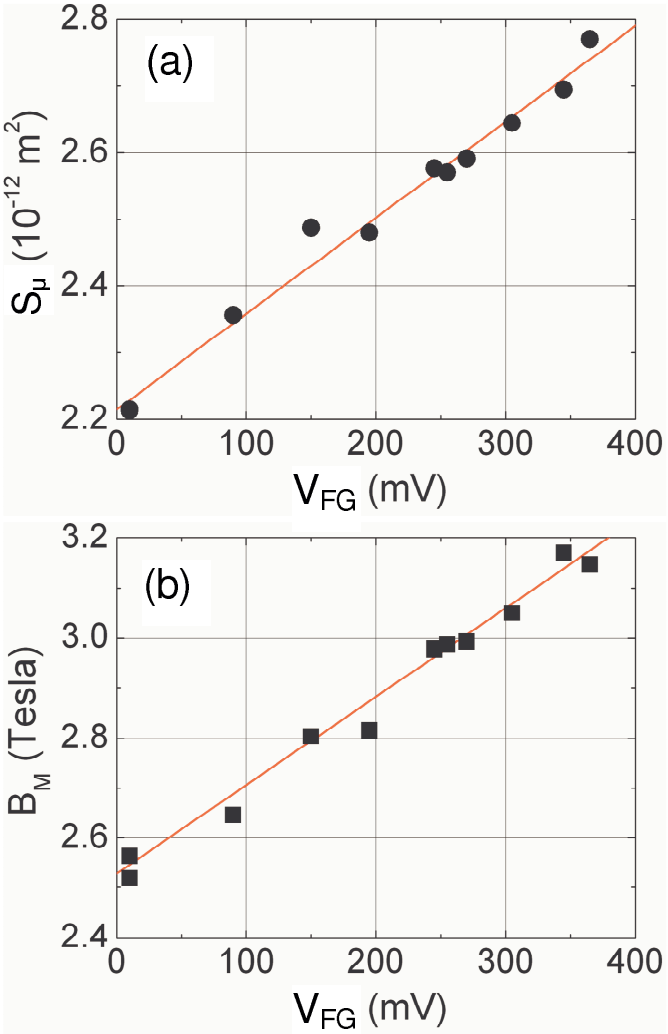

Figure 4.5: (a) The Aharonov-Bohm Area S_μ as a function of V_{FG}. (b) The dependence of midpoint field of oscillations B_M on V_{FG}.

Chapter 5

Detection of fractional statistics of Laughlin quasiparticles

The design of the interferometer devices allows us to study the statistical interactions between the Laughlin quasiparticles (LQPs) in an unambiguous way. From the measured AB oscillation data as a function of magnetic field and backgate voltage, the fractional statistics of LQPs can be directly calculated. In section 5.1 a brief introduction to fractional statistics of LQPs is presented. In section 5.2 we report experiments on an interferometer device with both the constrictions and the island on the $f = 1/3$ quantum Hall plateau. In section 5.3 we study an interferometer device in the regime with an $f = 2/5$ island embedded in the $f = 1/3$ quantum Hall fluid. We observe an Aharonov-Bohm superperiod of $\Delta_\Phi = 5h/e$, which has never been reported in any Aharonov-Bohm type interference experiment before.

5.1 Statistics of Laughlin quasiparticles

In three dimensional space, all fundamental "elementary" particles are either fermions or bosons. That is, upon exchange of two identical particles, the two-particle wave function acquires a phase factor of -1 for fermions or $+1$ for bosons. The particles are said to have statistics Θ if, upon exchange, the two-particle wave function acquires a phase factor $\exp(i\pi\Theta)$, and, upon a closed loop, a factor of $\exp(i2\pi\Theta)$. An exchange of two particles is equivalent to one particle executing a half loop around the other, so that a closed loop is equivalent to the exchange squared. The integer values $\Theta_B = 2j$ and $\Theta_F = 2j + 1$ describe the boson and fermion exchange statistics: $\exp(i2\pi j) = (-1)^{2j} = +1$ and $\exp[i\pi(2j + 1)] = (-1)^{2j+1} = -1$, respectively. Therefore, upon executing a closed loop, both types of particles produce a phase factor of $+1$, which

can be safely neglected in describing an interference experiment, such as the Aharonov-Bohm effect [10].

However, in two dimensional space, the laws of physics do not prohibit the existence of fractional statistics particles [5, 7], whose statistics can be any value between that of boson and fermion. Thus comes the name "anyons." This is because in two dimensions a closed loop executed by a particle around another particle is topologically distinct from a loop which encloses no particles, unlike the three dimensional case. Specifically, the low energy excitations of a fractional quantum Hall electron fluid (Laughlin quasiparticles) have a fractional charge [3, 4] and are expected to obey fractional statistics [6, 36]. Thinking in terms of a few such weakly interacting, fractional effective particles instead of in terms of very complex collective motions of all the underlying strongly interacting, integer statistics particles greatly simplifies description of the relevant physics.

Arovas, Schrieffer, and Wilczek [36] have used the adiabatic theorem to calculate the Berry phase [37] γ of a charge $e/3$ Laughlin quasiparticle at position $\Re$ encircling a closed path C containing another $e/3$ quasiparticle at $\Re'$ in the filling $f = 1/3$ FQH condensate,

$$\gamma = i \oint_C d\Re \left\langle \Psi(\Re, \Re') | \frac{\partial}{\partial \Re} \Psi(\Re, \Re') \right\rangle , \tag{5.1}$$

where Ψ is the many-electron Laughlin wave function [3, 13]. They found the difference

$$\Delta\gamma = 2\pi\Theta_{1/3} = 4\pi/3, \tag{5.2}$$

identified as the statistical contribution, between an "empty" loop and a loop containing another quasiparticle. It is possible to assign definite fractional statistics (mod 1) to quasiparticles of certain simple FQH fluids based only on the knowledge of their charge [38]. For example, for the one-electron layer FQH fluids corresponding to the main composite fermion sequence [39, 40] $f = p/(2jp + 1)$, with p and j positive integers, the charge $q = e/(2jp + 1)$ quasiparticle statistics is expected to be

$$\Theta_{p/(2jp+1)} = 2j/(2jp + 1) \ \ (\mathrm{mod}1). \tag{5.3}$$

5.2 $\nu = 1/3$ primary-filling Laughlin quasiparticle interferometer[1]

The interferometer consists of chiral edge channels coupled by quantum-coherent tunneling in two constrictions, thus enclosing an Aharonov-Bohm area. The two wide constrictions are designed not to be too constricted such that the constriction electron density is still close to the bulk density, allowing us to study the FQH regime in which the whole sample stays on the $f = 1/3$ QH plateau. This simpler regime, compared with the $f = 2/5$ embedded in $f = 1/3$ case covered in the next section, should help theoretical consideration of the quasiparticle interferometer physics. The observed flux and charge periods $\Delta_\Phi = h/e$ and $\Delta_Q = e/3$, respectively, correspond to the addition of one quasiparticle to the area enclosed by the interference path. The results are consistent with the Berry phase quantization condition that includes both Aharonov-Bohm and anyonic statistical contributions.

Interferometer devices were fabricated from low disorder AlGaAs/GaAs heterojunctions. After a shallow 140 nm wet etching, Au/Ti front-gate metal was deposited in the etch trenches, followed by liftoff, Figure 5.1. Samples were mounted on sapphire substrates with In metal, which serves as the back gate, and were cooled in a dilution refrigerator to 10.2 mK bath temperature, calibrated by nuclear orientation thermometry. Extensive cold filtering cuts the electromagnetic environment incident on the sample, allowing achievement of an electron temperature $\leq$ 15 mK in an interferometer device [44]. Four-terminal resistance $R_{XX} = V_X/I_X$ was measured with 50 pA ($f = 1/3$) or 200 pA ($f = 1$), 5.4 Hz ac current injected at contacts 1 and 4. The resulting voltage, including the interference signal, was detected at contacts 2 and 3.

The etch trenches define two 1.23 μm wide constrictions, which separate an approximately circular electron island from the 2D bulk. The shape of the electron density profile is largely determined by the etch trench depletion, illustrated in Figure 5.1(c). Moderate front-gate voltages V_{FG} are used to fine tune the constrictions for symmetry of the tunnel coupling and to increase the oscillatory interference signal. For the 2D bulk density $n_B = 1.25 \times 10^{11}$ cm^{-2} there are $\sim$3500 electrons in the island. The depletion potential has saddle points in the constrictions, and so has the resulting density profile.

In a quantizing field B, counterpropagating edge channels pass near the saddle points, where tunneling may occur. Thus, in the range of B where interference oscillations are observed, the filling of the edge channels is determined by the saddle point filling [46]. This allows one to determine the

[1] Published in F.E. Camino, Wei Zhou, and V.J. Goldman, Phys. Rev. Lett. **98**, 076805 (2007).

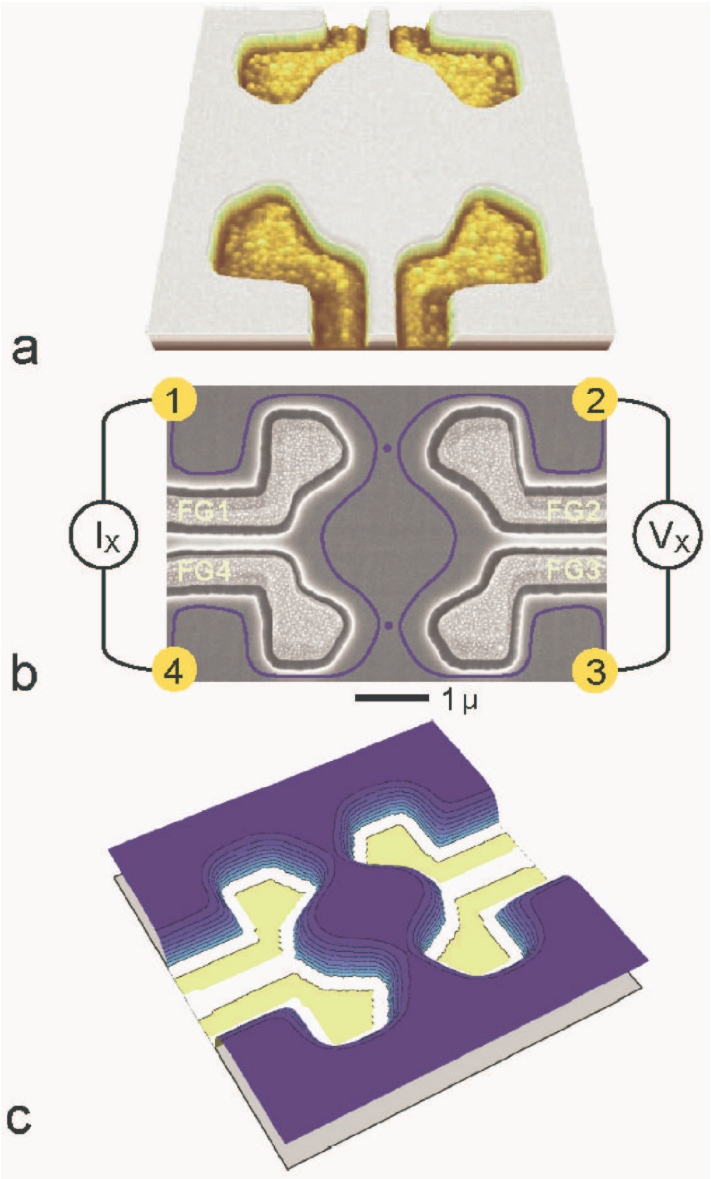

Figure 5.1: The interferometer sample. (a) Atomic force micrograph of the island region. (b) Scanning electron micrograph of the island region. Numbered circles represent Ohmic contacts at the four corners of the sample. Chiral edge channels (blue lines) are coupled in the constrictions by tunneling (shown as dots). (c) Illustration of the electron density profile. Note the saddle points in the two constrictions.

constriction density from the $R_{XX}(B)$ and $R_{XY}(B)$ magnetotransport, Figure 5.2. The Landau level filling $\nu = hn/eB$ is proportional to the electron density n in a given B. Thus the constriction ν is lower than the bulk ν_B. The island center n is estimated to be 3% less than n_B at $V_{FG} = 0$, the constriction-island center density difference is ∼7%. Thus, the whole island is on the same plateau for strong quantum Hall states with wide plateaus, such as $f = 1$ and 1/3. While ν is a variable, the quantum Hall exact filling f is a quantum number defined by the quantized Hall resistance as $f = h/e^2R_{XY}$.

In the integer quantum Hall regime, the Aharonov-Bohm ring is formed by the two counterpropagating chiral edge channels passing through the constrictions. Backscattering occurs by quantum tunneling at the saddle points in the constrictions, Figure 5.1, which complete the interference path. Relevant particles are electrons of charge $-e$ and Fermi statistics; thus, we can obtain an absolute calibration of the Aharonov-Bohm path area and the backgate action. Figure 5.3 shows conductance oscillations for $f = 1$, similar oscillations also occur for $f = 2$. The oscillatory conductance $\delta G = \delta R_{XX}/R_{XY}^2$ is calculated from R_{XX} data after subtracting a smooth background. The smooth background has two contributions: the bulk conduction at ν_B outside the bulk plateau regions, and the nonoscillatory interedge tunneling conductance in the interferometer. Extrapolated to $V_{FG} = 0$ [42, 46], the $f = 1$ magnetic field oscillation period is $\Delta_B = 1.86$ mT. This gives the interferometer path area $S = h/e\Delta_B = 2.22\ \mu\text{m}^2$, the radius $r = 840$ nm.

In the FQH regime, we observe the interferometric oscillations on the low-B side of the $f = 1/3$ plateau, Figure 5.3. This is the first experimental observation of $e/3$ quasiparticle interference oscillations when the island filling is 1/3 throughout. Extrapolated to $V_{FG} = 0$, the magnetic field oscillation period is $\Delta_B = 1.93$ mT. Assuming the flux period is $\Delta_\Phi = h/e$, this gives the interferometer path area $S = h/e\Delta_B = 2.14\ \mu\text{m}^2$, the radius $r = 825$ nm. The island edge ring area is determined by the condition that edge channels pass near saddle points in the constrictions. Classically, increasing B by a factor of ∼3 does not affect the electron density distribution in the island at all. Quantum corrections are expected to be small for a large island containing ∼3500 electrons. Indeed, the $f = 1/3$ interferometer path area is within ±3% of the integer value. Integer regime oscillations have an h/e fundamental flux period; we conclude that the flux period of 1/3 FQH oscillations is also $\Delta_\Phi = h/e$.

We use the back-gate technique [4, 29] to directly measure the charge period in the fractional regime. We calibrate the back-gate action $\delta Q/\delta V_{BG}$, where Q is the electronic charge within the Aharonov-Bohm path. The calibration

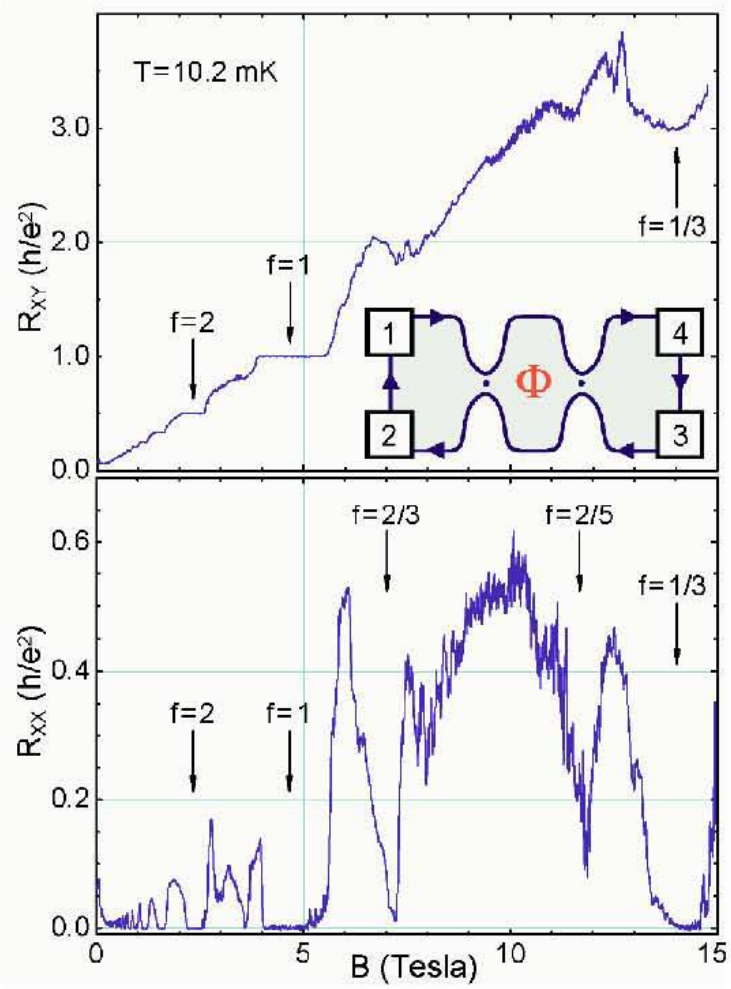

Figure 5.2: Directly measured diagonal R_{XX} and Hall R_{XY} resistance with $V_{FG} = 0$. Constriction fillings are determined from the values of the quantized plateaus. The fine structure is due to quantum interference effects in the residual disorder potential, including the interferometric conductance oscillations as a function of magnetic flux through the island. Inset: the chiral edge channel electron interferometer concept; dots show tunneling.

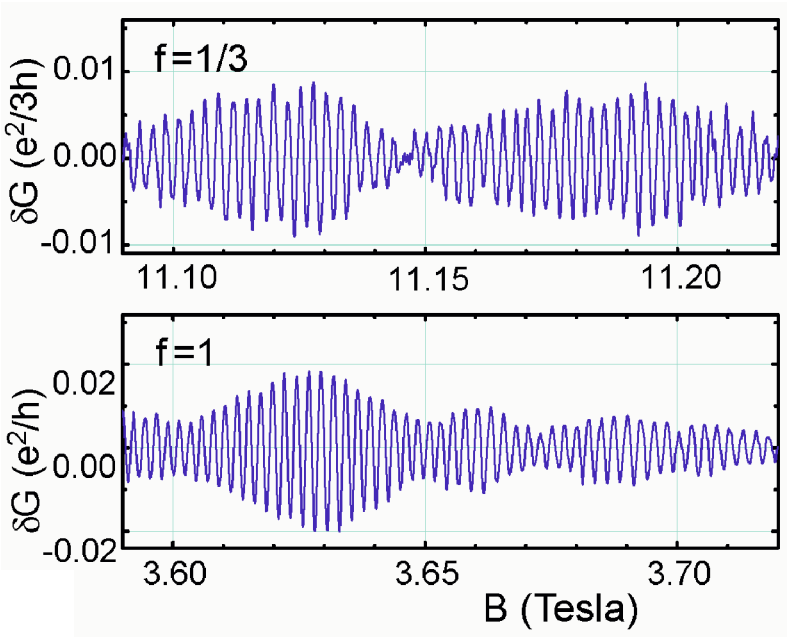

Figure 5.3: Representative interference conductance oscillations for electrons, $f = 1$, and for $e/3$ quasiparticles, $f = 1/3$. The magnetic flux period is $\Delta_\Phi = h/e$ in both regimes. Negative front-gate voltage, applied to increase the oscillation amplitude, shifts the oscillations to lower B.

is done by evaluation of the coefficient α in

$$\Delta_Q = \alpha(\Delta_{V_{BG}}/\Delta_B), \tag{5.4}$$

using the experimental oscillation periods, setting $\Delta_Q = e$ in the integer regime. Equation 5.4 normalizes the backgate voltage periods by the experimental B periods, approximately canceling the variation in device area, for example, due to a front-gate bias. The coefficient α is known *a priori* to a good accuracy in quantum antidots because the antidot is completely surrounded by quantum Hall fluid [4, 29]. In an interferometer, the island is separated from the 2D electron plane by front-gate etch trenches, so that its electron density is not expected to increase by precisely the same amount as n_B, requiring the calibration.

Figure 5.4 shows the conductance oscillations as a function of V_{BG} for $f = 1$ and $1/3$ and the analogous oscillations as a function of B. At each filling, the front-gate voltage is the same for the (vs. V_{BG}, vs. B) matched set. The $f = 1$ period $\Delta_{V_{BG}}$ corresponds to increment $\Delta_N = 1$ in the number of electrons within the interference path. We obtain $\Delta_{V_{BG}} = 315$ mV, $\Delta_B = 2.34$ mT, and the ratio $\Delta_{V_{BG}}/\Delta_B = 134.3$ V/T (front-gate $V_{FG} = -210$ mV for these data). This period ratio is 0.92 of that obtained in quantum antidots [29], as expected. For the 1/3 FQH oscillations, we obtain $\Delta_{V_{BG}} = 117.3$ mV, $\Delta_B = 2.66$ mT, and the ratio $\Delta_{V_{BG}}/\Delta_B = 44.1$ V/T (front-gate $V_{FG} = -315$ mV for these data). Using the integer calibration in the same device, the $e/3$ quasiparticle experimental charge period is $\Delta_Q = 0.328e$, some 1.7% less than $e/3$. To the first order, using the $\Delta_{V_{BG}}/\Delta_B$ ratio technique cancels dependence of the V_{BG} and B periods on the interferometer area and front-gate bias. The scatter of the quasiparticle charge values obtained from several matched data sets is $\pm 3\%$ in this experimental run.

These experimental results can be understood as follows [47–50]: The experimental periods are the same as in quantum antidots, comprising the addition of one quasiparticle. When filling $\nu < 1/3$, as in quantum antidots, the addition of flux h/e to an area occupied by the 1/3 condensate creates a quantized vortex, an $e/3$ quasihole. However, interferometric oscillations are observed to occur at filling $\nu > 1/3$, when quasielectrons are added to the condensate. This is consistent with the principal difference between the interferometer and the quantum antidots being that in antidots the FQH fluid surrounds electron vacuum, while the island contains the 1/3 fluid everywhere within the interference path in the present interferometer. The addition of flux reduces the number of $-e/3$ quasielectrons, the electron system is not the same as prior to flux addition, the added flux cannot be annulled by a singular gauge transformation [14, 51]. Another subtle difference is that a

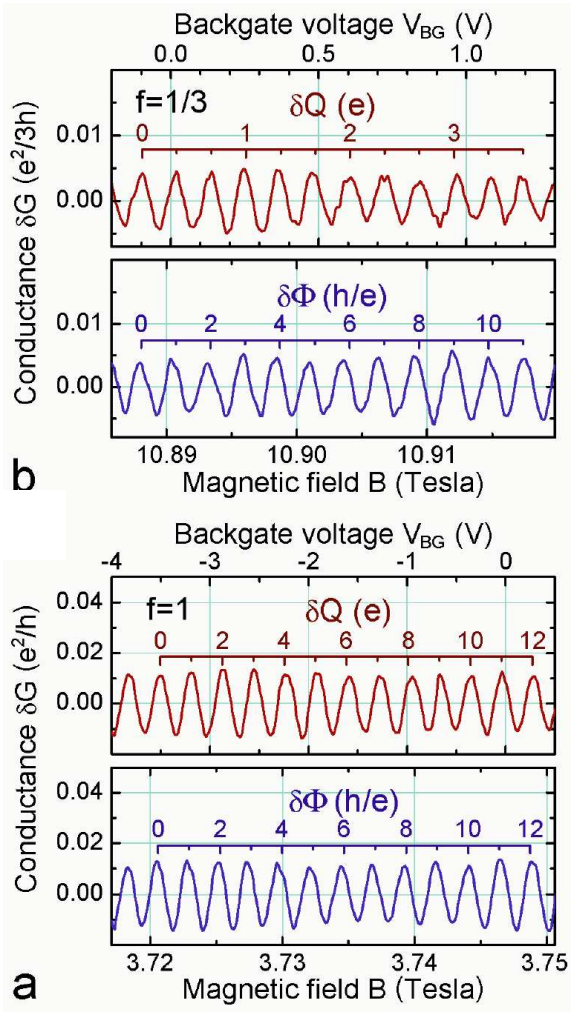

Figure 5.4: Matched backgate and magnetic field sweep data giving the $e/3$ charge period. (a) The interferometer device is calibrated using the conductance oscillations for electrons, $f = 1$. (b) This calibration gives the charge for the Laughlin quasielectrons $q = 0.33e$. The magnetic flux period $\Delta_\Phi = h/e$, the same in both regimes, implies anyonic statistics of the fractionally charged quasiparticles.

single quasihole can always be created in the 1/3 condensate, while the creation of a single quasielectron is not energetically favorable in a large, weakly confined, *isolated* FQH droplet [50, 52, 53]. Periods of $\Delta_\Phi = 3h/e$ and $\Delta_Q = e$ have been predicted in certain 1/3 FQH nonequilibrium models [47–49, 54].We therefore discuss experimental results via quasielectron configurations in the FQH ground state, as a more restrictive case.

In an unbounded FQH fluid, changing ν away from the exact filling f is accomplished by the creation of quasiparticles; the ground state consists of $\nu = f$ condensate and the matching density of quasiparticles [11–13]. Starting at $\nu = f$, changing magnetic field adiabatically maintains the system in thermal equilibrium, exciting quasiholes ($\nu < f$) or quasielectrons ($\nu > f$) out of the exact filling condensate. The equilibrium electron density, determined by the positively charged donors, is not affected. Confining potential breaks the quasiparticle-quasihole symmetry of the 2D system. Thus, in the interferometer, when the current-carrying edge channel has $\nu = f$, the island center has $\nu > f$ because electron density is greater in the same B, consistent with experimental observation of oscillations on the low-B side of the 1/3 plateau. Changing B also changes the flux $\Phi = BS$ through the area S enclosed by the interference path. In the experimental $\nu > 1/3$ regime, decreasing Φ by h/e increases the number of quasielectrons in S by one, $\Delta_N = 1$, and decreases by $+e/3$ the negative FQH condensate charge within S. The quasielectron is created out of the 1/3 condensate, the condensate density changes by $+e/3S$, the charge within the interference path does not alter and still neutralizes the positive donor charge.

This process can be described in terms of the Berry phase γ of the encircling $-e/3$ quasielectron, which includes the Aharonov-Bohm and the statistical contributions [36, 50]. When there is only one quasiparticle of charge $q = \pm e/3$ present, its orbitals are quantized by the Aharonov-Bohm condition $\gamma_m = (|q|/\hbar)\Phi_m = 2\pi m$ to enclose flux $\Phi_m = mh/|q|$ with $m = 0, 1, 2, ...$ These quantized quasiparticle orbitals enclose $-em$ of the underlying 1/3 condensate charge. When other quasiparticles are present, the Berry phase quantization includes a term describing braiding statistics of the quasiparticles, in addition to the Aharonov-Bohm phase. The total phase is quantized in increments of 2π:

$$\Delta_\gamma = (q/\hbar)\Delta_\Phi + 2\pi\Theta_{1/3}\Delta_N = 2\pi, \tag{5.5}$$

where $q = -e/3$ is the charge of the interfering quasielectron, and $\Theta_{1/3}$ is the statistics of the $-e/3$ quasielectrons. The first term in Eq. 5.5 contributes $(-e/3\hbar)(-h/e) = 2\pi/3$, the second term must contribute $4\pi/3$, giving an anyonic statistics $\Theta_{1/3} = 2/3$.

The same Berry phase equation describes the physically different process of

the island charging by the backgate. Here, in a fixed B, increasing positive V_{BG} increases the 2D electron density. The period consists of creating one $-e/3$ quasielectron out of the 1/3 condensate within the interference path, which causes the path to shrink by the area containing flux h/e. FQH fluid charge within the interference path does not neutralize the donors by $-e/3$. This is possible because the condensate is not isolated from the 2D bulk electron system, there is no Coulomb blockade, and the condensate charge within the interference path can increment by $+e/3$, any fractional charge imbalance ultimately supplied from the contacts. Thus, an $-e/3$ quasielectron is excited out of the condensate, $\Delta_N = 1$, the fixed condensate density is restored from the contacts, the interference path shrinks by area h/eB so that flux $\Delta_\Phi = -h/e$ in Eq. 5.5.

In conclusion, we realized a novel primary-filling $e/3$ quasiparticle interferometer where an $e/3$ quasiparticle executes a closed path around an island containing the 1/3 FQH fluid only. The central results obtained, the flux and charge periods of $\Delta_\Phi = h/e$ and $\Delta_Q = e/3$ are robust. Both the Aharonov-Bohm and the charging periods accurately correspond to the excitation of one $-e/3$ quasielectron within the interference path and are consistent with fractional statistics theories of interacting FQH quasiparticles.

5.3 Aharonov-Bohm superperiod[2]

The design of the interferometer device studied in this section allows a FQH regime where edge channels of the 1/3 FQH fluid encircle an island of the 2/5 fluid. We observe an Aharonov-Bohm superperiod of five magnetic flux quanta ($5h/e$), which has never been reported before in any system and is forbidden by the gauge invariance for a true Aharonov-Bohm geometry, where magnetic flux is added to a region of electron vacuum, as shown by Byers and Yang [55]. Our results do not violate the gauge invariance argument of the Byers-Yang theorem because the flux, in addition to affecting the Aharonov-Bohm phase of the encircling 1/3 quasiparticles, creates the 2/5 quasiparticles in the island. The AB superperiod is accordingly understood as imposed by the anyonic statistical interaction of Laughlin quasiparticles.

The samples were fabricated from low disorder AlGaAs/GaAs heterojunctions. After a shallow 140 nm wet etching, Au/Ti gate metal was deposited in etch trenches, followed by lift-off. Samples, mounted on sapphire substrates with In metal (serves as the backgate), were cooled to 10.2 mK in a dilution

[2]Published in F.E. Camino, Wei Zhou, and V.J. Goldman, Phys. Rev. B **72**, 075342 (2005), Phys. Rev. Lett. **95**, 246802 (2005).

refrigerator. Four-terminal resistance $R_{XX} = V_X/I_X$ was measured using a 100 pA, 5.4 Hz ac current.

The etch trench depletion potential defines two wide (1200 nm) constrictions, which separate an approximately circular electron island from the 2D bulk. The front-gate voltages V_{FG} are small, only fine-tuning the constrictions for symmetry. The electron density profile $n(r)$ in a circular island defined by etch trenches is evaluated following Refs. [42, 56]. For the 2D bulk density $n_B = 1.2 \times 10^{11}$ cm^{-2}, there are ∼1700 electrons in the island. The depletion potential has a saddle point in the constrictions, and so has the resulting density profile. In a quantizing magnetic field, tunneling between the counterpropagating edge channels (possible only over a few magnetic lengths ℓ_0) occurs near the saddle points. Thus, when Aharonov-Bohm oscillations are observed, the island edge channel filling is determined by the saddle point filling. From the magnetotransport, the saddle point density in the constrictions $n_C \approx 0.75 n_B$.

The local Landau level filling $\nu \equiv nh/eB$ is proportional to n; consequently, the constriction ν_C is lower than the bulk ν_B by ∼25% in a given B. While ν is a variable, the QH exact filling f, defined via the quantized Hall resistance as $f \equiv h/e^2 R_{XY}$, is a quantum number. Thus, there are two regimes possible: one when the whole sample has the same QH filling f, and another when there are two QH fillings: f_C in the constrictions, and f_B in the center of the island and in the 2D bulk. For example, there is a range of B where $f_C = f_B = 1$, illustrated in Figure 5.5(a). The second regime $f_C < f_B$, Figure 5.5(b), results in a *quantized* value [4, 20, 29, 57] of $R_{XX} = (h/e^2)(1/f_C - 1/f_B)$. A quantized plateau in $R_{XX}(B)$ implies QH plateaus for both the constrictions and the bulk, overlapping in a range of B and, in practice, provides definite values for both f_C and f_B. Such $R_{XX}(B)$ plateau occurs at $B \approx 12.35$ T for $f_C = 1/3$ and $f_B = 2/5$ ($n_C \approx 0.8 n_B$). However, $f_C = 1$ and $f_B = 2$, requiring $n_C \approx 0.5 n_B$, is not possible in this sample.

In the integer quantum Hall regime, the relevant particles are electrons of charge e and integer statistics; thus, we obtain an absolute calibration of the ring area and the backgate action of the interferometer. Figure 5.6 shows Aharonov-Bohm oscillations for $f_C = f_B = 1$ and 2 respectively. Conductance oscillations $\delta G = \delta R_{XX}/R_{XY}^2$ are calculated from the R_{XX} data after subtracting a smooth background. The Aharonov-Bohm ring is formed here by the edge channel circling the island, including two quantum tunneling links, Figure 5.5(c). The $f = 1$ period $\Delta_{B_1} \approx 2.81$ mT gives the area of the *outer* edge ring $S_O = h/e\Delta_{B_1} = 1.47$ μm^2, the radius $r_O \approx 685$ nm. The $f = 2$ period is very close: $2\Delta_{B_2} \approx 2.85$ mT gives the area $S_O \approx 1.45$ μm^2. The $f = 2$ fundamental period contains two oscillations, $2\Delta_{B_2} S_O = h/e$, because there

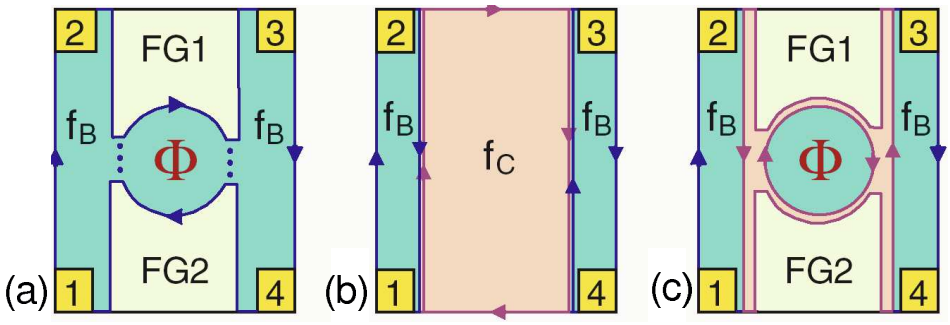

Figure 5.5: Illustrations of possible fillings for a sample with constrictions. Numbered squares are Ohmic contacts. (a) Both the bulk and the constrictions are on the same quantum Hall plateau. (b) A sample with constriction filling $f_C < f_B$ results in a quantized plateau $R_{XX} = (h/e^2)(1/f_C - 1/f_B)$. (c) The island and the bulk has the same filling f_B, while constriction filling $f_C < f_B$.

are two filled spin-polarized Landau levels. We calibrate the backgate action $\delta Q/\delta V_{BG}$ as described before. Figure 5.6 also shows oscillations as a function of V_{BG} for $f_C = f_B = 1$ and 2, respectively. The period $\Delta_{V_{BG}}$ corresponds to change $\Delta_N = 1$ in the number of electrons within the Aharonov-Bohm path. Thus $\Delta_{V_{BG}}$ should be the same for all spin-polarized QH states, provided the radius of the edge ring is constant; indeed, $\Delta_{V_{BG}} = 332$ mV for $f = 1$ and 342 mV for $f = 2$.

In the FQH regime, we focus on the regime when a 1/3 annulus surrounds an island of the 2/5 FQH fluid, Figure 5.5(c). Here, we observe Aharonov-Bohm oscillations with period $\Delta_B \approx 20.1$ mT, Figure 5.7. The period gives the *inner* edge ring area $S_I = 5h/e\Delta_B \approx 1.03\ \mu\text{m}^2$, radius $r_I \approx 570$ nm. Figure 5.7 also shows the oscillations as a function of V_{BG}, the period $\Delta_{V_{BG}} \approx 937$ mV. We are confident that current flows through the $f_C = 1/3$ region separating two $f_B = 2/5$ regions with Ohmic contacts because $R_{XX}(B)$ exhibits a plateau at $h/2e^2$, Figure 5.8. The island density is 4% less than n_B [42]; thus, island ν the same as ν_B occurs at 4% lower B. The ratio of the periods $\Delta_B/\Delta_{V_{BG}} \propto N_\Phi/N_e = 1/f$ is independent of the Aharonov-Bohm ring area. N_Φ and N_e are the number of flux quanta and electrons within the Aharonov-Bohm path area. The fact that the ratios fall on a straight line forced through zero confirms the island filling $f = 2/5$ at 11.9 T, Figure 5.8.

The striking feature of the oscillations in Figure 5.7 is the Aharonov-Bohm period of five fundamental flux quanta: $\Delta_\Phi = 5h/e$. To the best of our knowledge, such a superperiod of $\Delta_\Phi > h/e$ has never been reported before. Addition of flux h/e to an area occupied by the 1/3 FQH condensate creates a

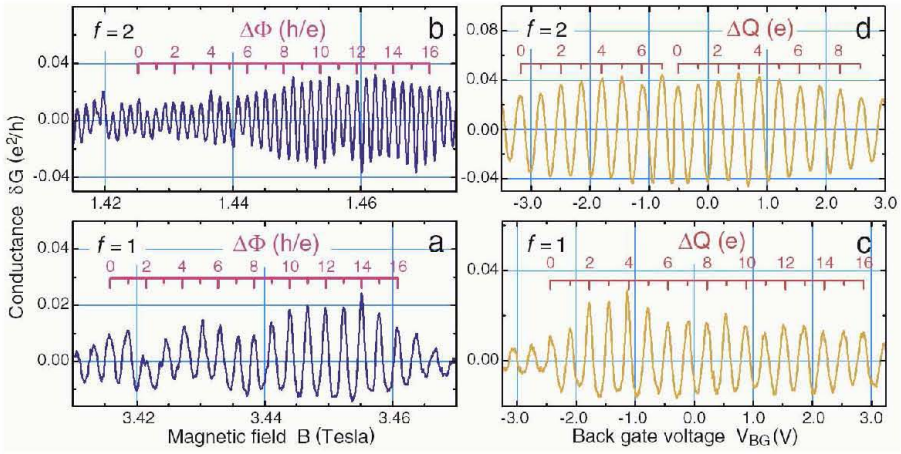

Figure 5.6: Interference of electrons in the integer QH regime. (a),(b) AB oscillations in conductance when one ($f = 1$) or two ($f = 2$) Landau levels are filled. The flux period $\Delta_\Phi = h/e$ gives the outer edge ring radius 685 nm. (c),(d) Positive V_{BG} attracts 2D electrons one by one to the area within the AB path, modulating the conductance. This calibrates the increment $\Delta_{V_{BG}}$ needed to increase the charge by $\Delta_Q = e$. Note that $\Delta_{V_{BG}}$ is independent of f.

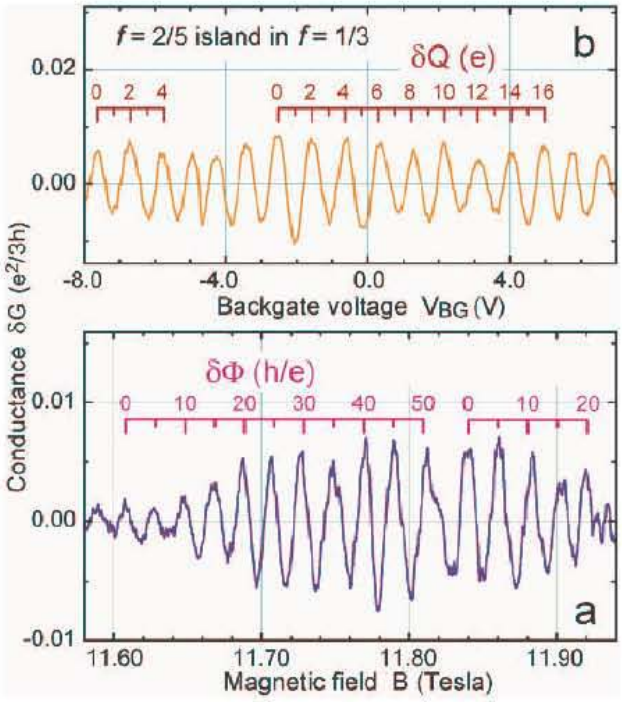

Figure 5.7: Oscillatory conductance for $e/3$ quasiparticles circling an island of $f = 2/5$ FQH fluid. (a) Flux through the island period $\Delta_\Phi = 5h/e$ corresponds to creation of ten $e/5$ quasiparticles in the island [one h/e excites two $e/5$ quasiparticles from the 2/5 FQH condensate, the total (quasiparticles + condensate) charge is fixed]. Such superperiod $\Delta_\Phi > h/e$ has never been reported before. (b) The charge period $\Delta_Q = 2e$ confirms that the $e/3$ quasiparticle consecutive orbits around the 2/5 island are quantized by a condition requiring increment of ten $e/5$ quasiparticles.

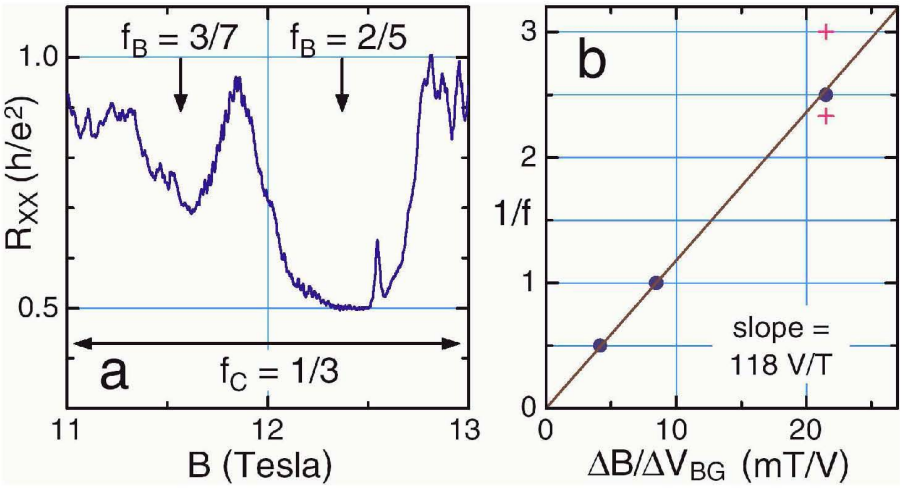

Figure 5.8: (a) Magnetoresistance of the interferometer sample at 10.2 mK. The horizontal arrow shows approximately the $f_C = 1/3$ plateau. Note the *quantized* plateau $R_{XX}(B) = h/2e^2$ at 12.35 T, obtainable only with $f_C = 1/3$, $f_B = 2/5$. (b) The oscillation period ratio for the data of Figures 5.6 and 5.7. $\Delta_B/\Delta_{V_{BG}} \propto 1/f$, independent of the AB path area. The straight line goes through (0, 0) and the $f = 1$ point. Experimental $\Delta_B/\Delta_{V_{BG}}$=21.4 mT/V gives the island filling $f = 2/5$. The crosses (the nearest FQH effect $f = 3/7$ and 1/3) do not fit the data.

vortex, an $e/3$ quasihole [3, 13]. Likewise, addition of flux h/e to the 2/5 FQH fluid creates two vortices, that is, two $e/5$ quasiholes [18]. These predictions have been verified at a microscopic level in quantum antidot experiments [4, 29]. Thus, addition of $5h/e$ to the $f = 2/5$ island creates ten $e/5$ LQPs with total charge $\Delta_Q = 2e$, confirmed by the backgate data, Figure 5.7. In contrast, the periods observed in quantum antidots correspond to addition of one LQP only, for both the 1/3 and 2/5 cases. The principal difference between the present interferometer and the antidots is that in quantum antidots the FQH fluid surrounds electron vacuum, while in the present interferometer the 1/3 fluid surrounds an island of the 2/5 fluid. The gauge invariance argument [51, 55] requiring h/e for the true AB geometry is not applicable here because the interior of the AB path contains electrons, and applied flux creates LQPs in the island. Addition of flux does excite LQPs, the system is not the same as prior to flux addition; thus, the applied flux cannot be annulled by a singular gauge transformation. Likewise, Laughlin's "gedanken experiment" cannot be applied to the interferometer geometry to assume that any charge is transferred in or out of the island by the AB flux.

Any viable interpretation must conform to the experimental facts: (i) current is transported by $e/3$ LQPs of the surrounding 1/3 fluid, Figure 5.8(a). (ii) The oscillations originate in the 2/5 island, Figure 5.8(b). (iii) Both flux (no systematic net charging of the island) and backgate (systematic charge transfer into the island) periodic oscillations must be accounted for at least 10 periods away from exact filling, Figure 5.7. (iv) The oscillations are found to be robust, observed in four distinct cooldowns, persisting to 140 mK and upon application of a moderate front gate voltage ± 300 mV [46]. (v) We have observed similar integer and fractional AB oscillation data in another sample with a larger lithographic $R \approx 1300$ nm [42]. $\Delta_{B_{2/5}} \approx 6.4\Delta_{B_1}$ is consistent, upon the same depletion potential analysis, with the period $\Delta_\Phi = 5h/e$.

A different r_I would yield a different Δ_Φ. We restrict analysis to Δ_Φ of simple rational multiples of h/e, consistent with the particle nature of charged elementary excitations. The observed field period $\Delta_{B_{2/5}} \approx 7.15\Delta_{B_1}$, the facts that current flows in the outer edge channels with $f_C = 1/3$, and that experimental $\Delta_B/\Delta_{V_{BG}}$ gives the filling 2/5, are all consistent with formation of an $f = 2/5$ island within the 1/3 outer edge ring, the inner ring radius $r_I < r_O$. This is also expected since the island center density $n_I \approx 1.22 n_C$, just above the assigned $f_I \approx 1.20 f_C$. The alternative $\Delta_\Phi = 5h/2e$, $\Delta_Q = e$ (still constituting an AB superperiod) is ruled out as giving too small $r_I \approx 400$ nm. The confining potential at $r_I \approx 400$ nm is simply too weak to support a *stable* edge ring; an estimate using models [42, 56] gives an order of magnitude weaker gradient $dn(r)/dr$ at 400 nm than at 570 nm. The alternative of $\Delta_\Phi = h/e$,

$\Delta_Q = 2e/5$ gives yet smaller $r_I = 255$ nm, where confining potential is nearly flat and thus cannot define an edge channel. Another consideration is tunneling through the distance $t = r_O - r_I$, between the inner and the outer edge channels. The LQP tunneling rate is estimated [58] as $\sim \exp[-(t/2\sqrt{3\pi}\ell_0)^2]$, which gives 10^{-2} for $r_I \approx 570$ nm (agreeing with experiment, Figure 5.7) and 10^{-14} for $r_I \approx 400$ nm, much too small to observe.

Exchange of charge between the island and the surrounding FQH fluid in increments of one LQP, $\Delta_Q = e/5$ (as in quantum antidots) is clearly not consistent with the data. A model where no LQPs are created (only exact filling FQH condensates are considered), but instead the $1/3-2/5$ condensate boundary shifts [59], is not energetically feasible. As is well known, in a large FQH fluid, changing ν away from the exact filling f is accompanied by creation of LQPs, so as to maintain average charge neutrality; the ground state consists of a $\nu = f$ condensate and the matching density of LQPs [3, 6, 18, 29]. Forcing exact filling (and no LQPs) at $B \neq B_f \equiv hn/ef$ changes n away from the equilibrium value determined by the positively charged donors. In present geometry, this would lead to formation of a charged $\nu = f = 2/5$ disk surrounded by an oppositely charged 1/3 annulus, and thus huge Coulomb energy. For the tenth oscillation from the exact filling, the net charge is $20e$, the charging energy $\sim$1000 K, much more than the LQP gap. An intermediate model where LQPs are allowed, but are envisioned concentrated near the $1/3-2/5$ boundary, besides still present charging energy (additional to the equilibrium ground state energy), must overcome the difficulty of the local ν being affected. Concentrating 100 of $e/5$ LQPs within $5\ell_0$ of r_I changes local filling to $\nu = 0.528 > 1/2$, well outside the 2/5 plateau. This would certainly break the observed AB periodicity.

In the interferometer, if we neglect the symmetry properties of the FQH fluids, in the absence of a Coulomb blockade, there is no *a priori* constraint that the total charge of the 2/5 island be quantized in units of e, much less in units of $2e$. The island fluid could adjust in increments of one LQP, any fractional charge imbalance supplied from the contacts. Thus the periods $\Delta_\Phi = 5h/e$, $\Delta_Q = 2e$ must be imposed by the symmetry properties of the two FQH fluids. Recently Goldman has proposed a microscopic model [50] based on the Haldane-Halperin fractional statistics hierarchical construction [6, 18] of the 2/5 condensate. In the model, the 2/5 QH condensate is viewed as a "max density droplet" (MDD) condensate of $-e/3$ quasielectrons on top of the 1/3 QH condensate, and the Aharonov-Bohm superperiod corresponds to increment by one of the MDD quasielectron and concurrently excitation of 10 $e/5$ quasiholes out of the 2/5 island condensate. Thus the Berry phase

quantization condition is

$$\Delta_\gamma = \frac{q}{\hbar}\Delta_\Phi + 2\pi(\Theta_{1/3}\Delta_{N_{1/3}} + \Theta_{2/5}^{-1/3}\Delta_{N_{2/5}}) = 2\pi. \tag{5.6}$$

Substitute $q = -e/3$, $\Delta_\Phi = 5h/e$, $\Delta_{N_{1/3}} = 1$ and $\Delta_{N_{2/5}} = 10$, we obtain

$$\frac{\Delta_\gamma}{2\pi} = -\frac{5}{3} + \Theta_{1/3} + 10\Theta_{2/5}^{-1/3} = 1. \tag{5.7}$$

The two concurrent physical processes, the increment of one MDD quasielectron and excitation of 10 $e/5$ quasiholes in the 2/5 island, suggest to interpret Eq. 5.7 as two separate equations: $1/3 + \Theta_{1/3} = 1$ and $10\Theta_{2/5}^{-1/3} = 2$. These give $\Theta_{1/3} = 2/3$ and $\Theta_{2/5}^{-1/3} = 1/5$.

In conclusion, we realized a novel Laughlin quasiparticle interferometer, where an $e/3$ LQP executes a closed path around an island of the 2/5 FQH fluid. The central results obtained, the Aharonov-Bohm superperiods of $\Delta_\Phi = 5h/e$ and $\Delta_Q = 2e$ are robust. These results do not violate the Byers-Yang theorem, and are interpreted as due to anyonic braiding statistics of LQPs.

Chapter 6

Properties of the Aharonov-Bohm superperiod

The Aharonov-Bohm superperiod of magnetic flux $5h/e$ observed in the FQH regime, where quasiparticles of the 1/3 FQH fluid execute a closed path around an island of the 2/5 fluid, implies anyonic statistics of Laughlin quasiparticles. In this chapter, we study the properties of the superperiodic oscillations by measuring their dependence on front-gate voltage and temperature. The results obtained further strengthen our previous conclusions about the superperiods and also shed some light on the proposed fault-tolerant quantum computation with anyons [9, 60, 61].

6.1 Flux-period scaling in the Laughlin quasiparticle interferometer[1]

The front-gates of the Laughlin interferometer device are formed by depositing Au/Ti metals into etch trenches. The electric potential of the front-gates adds to that produced by the etch trenches, and affects the island electron density profile. We find a linear dependence of the Aharonov-Bohm period on front-gate voltage for electrons (integer filling $f = 1$) and for Laughlin quasiparticles (fractional 2/5 embedded in 1/3). Comparing the experimental data for both regimes and for two samples, we find the magnetic field period and its slope scale with the radius of the Aharonov-Bohm orbit. Analysis of the directly measured integer and fractional slope data allows us to determine the interferometer area in the fractional regime, and thus the Laughlin quasiparticle

[1] Published in Wei Zhou, F.E. Camino, and V.J. Goldman, Phys. Rev. B **73**, 245322 (2006).

flux period of $5h/e$, within the experimental accuracy.

The quantum electron interferometer samples were fabricated from a low disorder GaAs/AlGaAs heterojunction material where 2D electrons (285 nm below the surface) are prepared by exposure to red light at 4.2 K. The four independently contacted front gates were defined by electron beam lithography on a pre-etched mesa with Ohmic contacts. After a shallow 140 nm wet chemical etching, Au/Ti gate metal was deposited into the etch trenches (lithographic radius $R \approx 1050$ nm, Sample M97Bm), followed by lift-off, see Figure 6.1. Samples were mounted on sapphire substrates with In metal, which serves as a global backgate. Samples were cooled to 10.2 mK; four-terminal resistance $R_{XX} = V_X/I_X$ was measured by passing $50 - 200$ pA, 5.4 Hz ac current through contacts 1 and 4, and detecting the voltage between contacts 2 and 3 by a lock-in-phase technique. The four front gates are deposited into etch trenches. Even when front gate $V_{FG} = 0$, the GaAs surface depletion of the etch trenches creates electron confining potential, defining two wide constrictions, which separate an approximately circular 2D electron island from the 2D "bulk," Figure 6.1. The electron density profile $n(r)$ in a circular island resulting from the etch trench depletion can be evaluated using the model of Ref. [42], based on Ref. [56], see Figure 6.2. For the bulk density $n_B = 1.2 \times 10^{11}\text{cm}^{-2}$, there are $\sim$2000 electrons in the island. Comparison with a Hartree-Fock profile shows that quantum corrections are significant only for $n < 0.4n_B$ low density tails, outside the AB path area. However, the overall density profile follows the $B = 0$ profile in order to minimize the large Coulomb charging energy arising from deviations from the donor-neutralizing $B = 0$ profile. The depletion potential has a saddle point in the constriction region, and so has the resulting electron density profile. From the magnetotransport, we estimate the saddle point density to be 0.72 n_B. Note that the island center density is slightly (several percent) lower than the 2D bulk density.

On the integer ($f = 1$) and fractional (2/5 embedded in 1/3) quantum Hall plateaus, we acquire the Aharonov-Bohm oscillation data as reported previously. By varying the front-gate voltage V_{FG}, we observe the B-field position of the oscillations shift and their period Δ_B change; see Figure 6.3. The effect of the front-gate bias is two fold. The larger effect is the transistor action affecting the overall 2D electron density in the several μm neighborhood of the gates, including the entire island. This is so because at every point in the 2D plane, the electric potential has contributions from the entire (equipotential) front-gate metal area, including the long gate voltage leads, because of the poor screening of the gate electric field by 2D electrons. The overall decrease in the electron density (negative V_{FG}) is evidenced by the systematic shift to

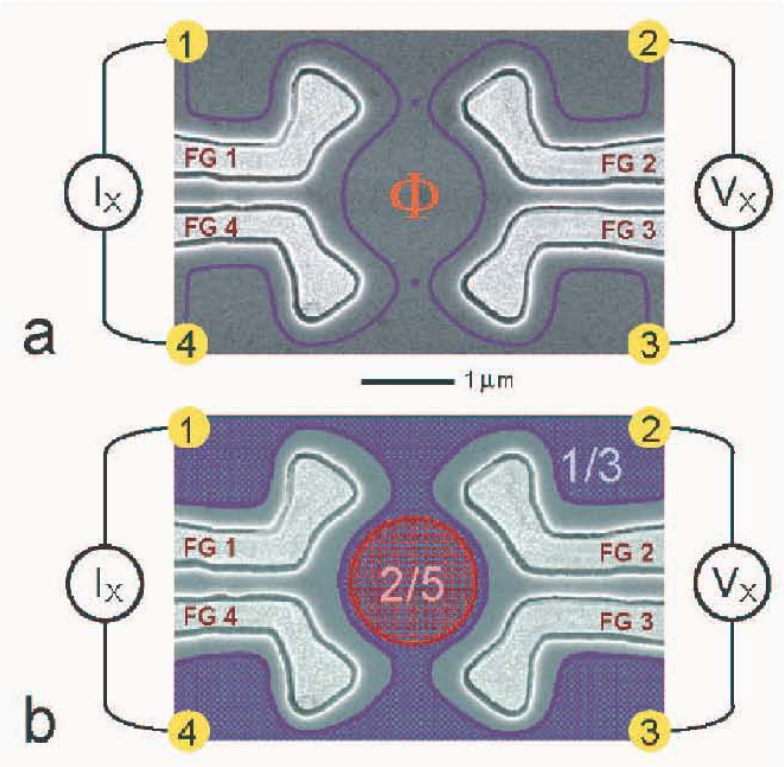

Figure 6.1: Scanning electron microscope image of the sample. The nearly circular island is defined by four front gates, FG1−FG4. Numbered circles are Ohmic contacts. (a) In the IQH regime, the whole sample is on the same QH plateau. Counterpropagating edge channels (blue lines) are coupled by tunneling (blue dots) in the constrictions. (b) In the FQH regime, an $f = 2/5$ island is enclosed by $f = 1/3$ QH fluid.

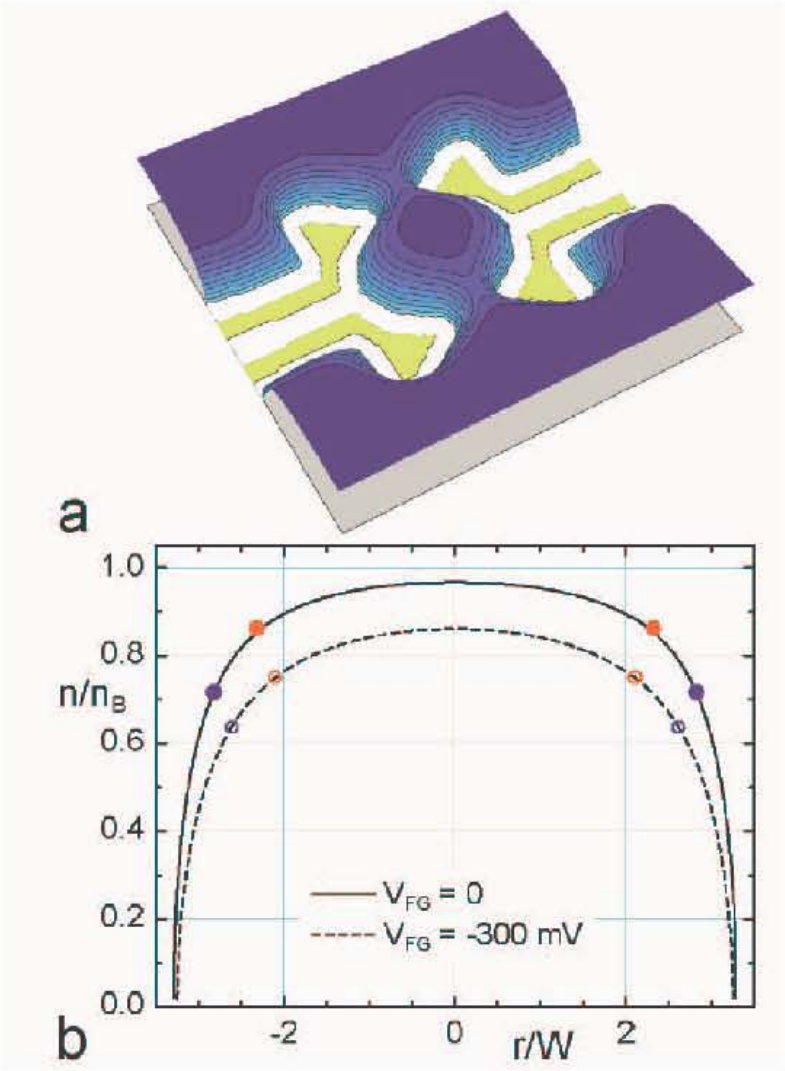

Figure 6.2: (a) A qualitative illustration of the 2D electron density profile. (b) The calculated electron density profile in a circular island defined by an etched annulus of inner radius $R \approx 1050$ nm, $n_B = 1.2 \times 10^{11}$ cm^{-2}. The calculation follows the $B = 0$ model of Ref. [42]. $W = 245$ nm is the depletion length parameter. The blue circles give the radius of the outer edge ring $r_{Out} \approx 685$ nm, obtained from the integer Aharonov-Bohm period and $n(r_{Out})$ from the B-field position on the constriction QH plateaus. The red circles give the inner edge ring radius $r_{In} \approx 570$ nm, obtained with the fractional $N_\Phi = 5$ and the density ratio $n(r_{In})/n(r_{Out}) = (2/5)/(1/3) = 1.20$.

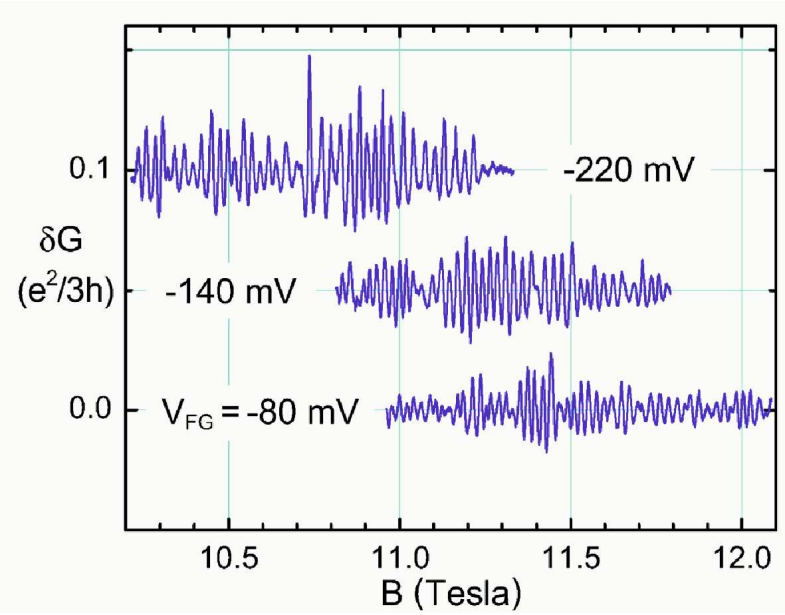

Figure 6.3: Aharonov-Bohm conductance oscillations δG as a function of B for several values of front gate voltage V_{FG}, given in the labels next to each trace. All the traces are for $f = 1/3$ FQH fluid circling an $f = 2/5$ island, and have been shifted vertically in steps of $0.05e^2/3h$. Each trace contains $\sim$40 oscillations with a well defined period Δ_B, which depends on V_{FG}.

a lower B of the constriction QH plateau (with Aharonov-Bohm oscillations superimposed).

In addition, the front gates modify the island and the constriction electron density profile by affecting the primary confining potential of the etch trenches. Since tunneling amplitude is exponentially sensitive to the tunneling distance, the position of the tunneling links at the saddle points in the constrictions is nearly fixed. The constrictions' saddle-point electron density determines the equipotential contour of the Aharonov-Bohm path in the island. As evidenced by the systematic increase of the period Δ_B (decrease of island area, negative V_{FG}), the saddle-point electron density decreases proportionately less than the island density. Accordingly, remaining on the same quantum Hall plateau, the island edge channels must follow the constant electron density contours with density equal that in the constrictions and move inward, towards the island center, and the AB path area shrinks. Thus, the electronic charge within the AB path area decreases because the overall island density decreases, and also because the area itself decreases.

The dependence of the Aharonov-Bohm field period Δ_B on the front-gate voltage V_{FG} for electrons ($f = 1$) and for Laughlin quasiparticles (2/5 embedded in 1/3) is shown in Figure 6.4. The integer data contains two sets of points from two distinct cooldowns, with ∼7% different 2D electron density, appropriately scaled to produce equal $\Delta_B(V_{FG} = 0)$. We observe an approximately linear dependence $\Delta_B = \Delta_B(0) + (d\Delta_B/dV_{FG})V_{FG}$ in the range of moderate V_{FG} studied; the solid lines are the least squares fits to $\Delta_B = a + bV_{FG}$.

The directly measured Δ_B and the slope, $d\Delta_B/dV_{FG}$, and the assumed Aharonov-Bohm area S can be combined to give $V_{FG}(1e)$, the front-gate voltage attracting charge $1e$ to the area. Capacitance of the island is modeled as that of a 2D disk with radius r, and defined by $C \equiv Q/V = e/V_{FG}(1e)$. For a 2D disk of radius r, the classical capacitance is approximately proportional to r, neglecting a slowly varying logarithmic term. For a large (∼2000 electrons) 2D island, the quantum corrections to the classical capacitance are small, and the product $rV_{FG}(1e)$ should be approximately constant, independent of the quantum Hall filling or the area. Therefore, we analyze the data as follows (the analysis aims to express quantities of interest in terms of directly measured quantities and fundamental constants only). As is well known, the Aharonov-Bohm effect is a topological, nonlocal periodic dependence of the phase of a particle's wave function on magnetic flux enclosed by the particle's closed path. In experiment, the interferometer devices are located in a region of a uniform magnetic field, thus observation of AB effect implies existence of a well-defined closed path that determines the enclosed flux. On the same quantum Hall plateau, the Aharonov-Bohm magnetic flux period is N_Φ fundamental flux quanta, $\Delta_\Phi = N_\Phi h/e$ (note that the number N_Φ is not assumed to be an integer here). The AB path encloses area S, defining the fundamental magnetic flux period

$$\Delta_\Phi = \Delta_B S = N_\Phi h/e, \tag{6.1}$$

thus $S = N_\Phi h/e\Delta_B$. Differentiating Eq. 6.1 with respect to front-gate bias, we obtain

$$[(d\Delta_B/dV_{FG})S + (dS/dV_{FG})\Delta_B]_f = 0. \tag{6.2}$$

The subscript here denotes the same quantum Hall plateau. Substituting $S = N_\Phi h/e\Delta_B$ into Eq. 6.2 gives

$$dS/dV_{FG} = -(d\Delta_B/dV_{FG})(N_\Phi h/e\Delta_B^2). \tag{6.3}$$

On the other hand, as is well known, an electron occupies the area $S_1 = 2\pi\ell_0^2 = h/eB$ per spin-polarized Landau level. Thus, Landau level density of electron states is $S_1 = h/eB_1$, where B_1 is the magnetic field where the exact filling $\nu = f = 1$ occurs. This expression for S_1 can also be obtained by

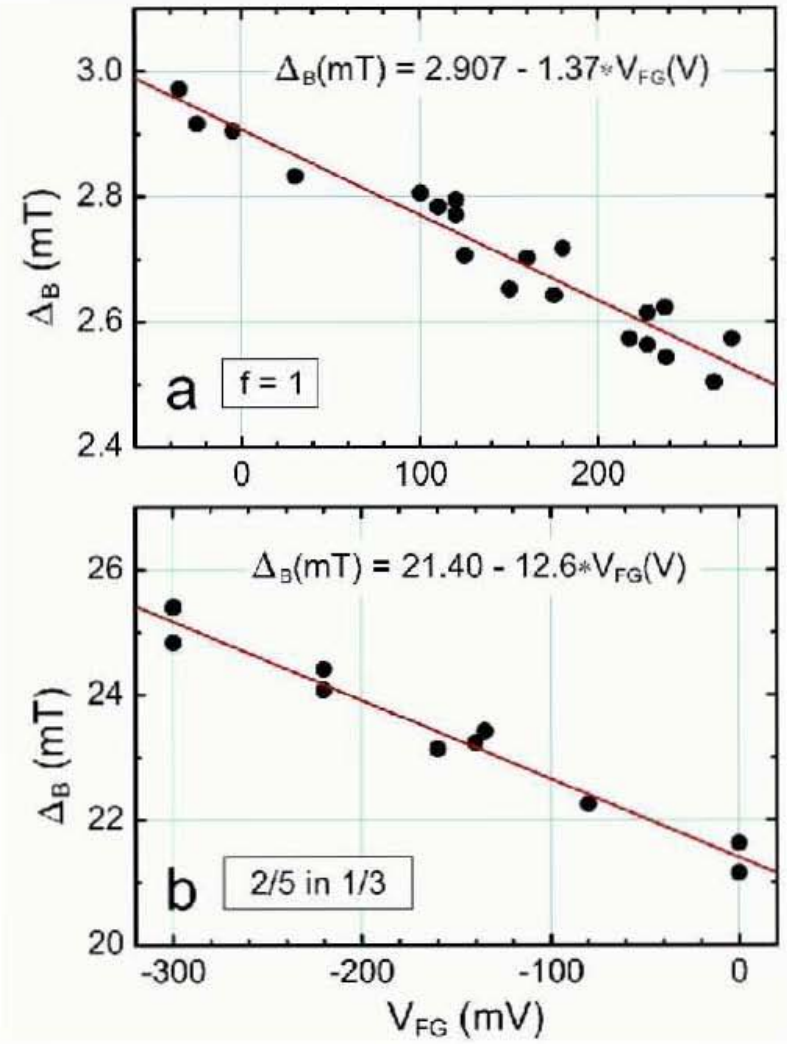

Figure 6.4: Dependence of the Aharonov-Bohm period Δ_B on front-gate voltage V_{FG} for (a) $f = 1$ and (b) $f = 2/5$ embedded in $f = 1/3$. The dependence is approximately linear in the range of V_{FG} studied; the solid lines are least squares fits. The $\Delta_B(V_{FG} = 0)$ values give the A-B path areas $S_{Out} = h/e\Delta_B = 1.42 \times 10^{-12}$ m^2 ($f = 1$) and $S_{In} = 5h/e\Delta_B = 0.966 \times 10^{-12}$ m^2 (2/5 embedded in 1/3).

noticing that physically the one-electron area is the inverse of the electron areal density: $S_1 = 1/n$. Recalling that Landau level filling factor $\nu = nh/eB$, we again obtain the one-electron area $S_1 = h/\nu eB = h/eB_1$. We define $V_{FG}(1e)$ as the front-gate voltage required to attract charge $1e$ to the AB path area. Linearizing Eq. 6.3 for $V_{FG}(1e)$, $dS/dV_{FG} = S_1/V_{FG}(1e)$, and substituting $S_1 = h/eB_1$, we obtain

$$V_{FG}(1e) = -\frac{\Delta_B^2}{(d\Delta_B/dV_{FG})N_\Phi B_1}. \tag{6.4}$$

Note that the derivative $d\Delta_B/dV_{FG}$ is negative, and that linearization of Eq. 6.3 is justified by the large size of the electron island, because $1/N_e \approx 1/2000$ is small.

Some discussion on how Eq. 6.4 applies to the present experimental situation is in order. In the experiment, the sample is located in a uniform magnetic field B, which is being slowly varied. The observation of an AB oscillatory signal thus implies existence of a well-defined AB area, since the Aharonov-Bohm effect is nonlocal and topological in nature and is oscillatory not in B, but in magnetic flux through a closed path, which defines the enclosed area (Stokes' theorem). The directly measured period Δ_B and slope $d\Delta_B/dV_{FG}$ in Eq. 6.4 refer to the same AB flux period which is being determined here, so that any visualization of the experimental situation in terms of edge channels is only illustrative and is presented as a physically viable model. The derivation of Eqs. 6.1–6.4 does not depend on details of a particular edge channel model used for physical visualization. Thus, Eq. 6.4 is not sensitive to electron density distribution inside or outside the AB path, N_Φ appears in Eq. 6.4 only because we express Δ_Φ in units of h/e.

In an electron system where density is not constant, relation $S_1 = 1/n = h/eB_1$ is still locally valid on a scale of area containing several electrons, that is, several ℓ_0^2. Density n and the $\nu = 1$ field B_1 in Eq. 6.4 refer to the actual AB path, that is, to the edge channel giving rise to the oscillatory conductance signal. In the integer $f = 1$ regime, n and B_1 thus refer to the only existing edge channel; B_1 (extrapolated to $V_{FG} = 0$) is determined as the field at which $\nu = 1$ occurs for the constriction (not the bulk) QH plateau, on which the $f = 1$ AB signal is superimposed. Thus determined B_1 is also used in the fractional (2/5 embedded in 1/3) regime, where it therefore refers to the $f = 1/3$ edge channel, which carries the transport current (Hall resistance plateau is at $3h/e^2$), and where the fractional AB signal originates. This is justified because the edge channel giving rise to the AB signal must pass through the constrictions, and the corresponding density is thus determined by the saddle point density in the constrictions, as discussed previously. Thus,

Table 6.1: Summary of results obtained from the experimental Aharonov-Bohm period Δ_B and its dependence on front-gate voltage V_{FG}. Sample M61Dd data is from Ref. [42].

Sample	M97Bm ($f = 1$)	M97Bm (2/5 in 1/3)	M61Dd ($f = 1$)
$\Delta_B(0)$, mT	2.907	21.40	1.872
$d\Delta_B/dV_{FG}$, mT/V	−1.37	−12.6	−1.22
B_1, T	3.92	3.92	2.53
$V_{FG}(1e)$, mV	1.58	1.86	1.14
r, nm	673	555	839
$rV_{FG}(1e)$, V·nm	1.06	1.03	0.956

the physical interpretation of Eq. 6.4 is that it describes effective electrostatic coupling to the front gates of electrons located at the position of the AB path.

The experimentally determined field periods $\Delta_B(V_{FG} = 0)$, their slopes $d\Delta_B/dV_{FG}$, and B_1 for two samples are summarized in Table 6.1. Eq. 6.4 is used to obtain $V_{FG}(1e)$ and the product $rV_{FG}(1e)$ assuming $N_\Phi = 5$ for the fractional Hall regime. The integer $N_\Phi = 1$; the AB path radius r assumes a circular path, alternatively S can be used instead of r. Note that using $N_\Phi = 5$ for the inner 2/5 in 1/3 island gives roughly equal $V_{FG}(1e)$; the products $rV_{FG}(1e)$ are equal (within the experimental uncertainty of ±10%), as expected. Assuming different N_Φ gives correspondingly different fractional $V_{FG}(1e) \propto 1/N_\Phi$ and $rV_{FG}(1e) \propto 1/\sqrt{N_\Phi}$, inconsistent with the expectation. For example, using the next physically feasible flux period $\Delta_\Phi = 5h/2e$ ($N_\Phi = 2.5$) increases the fractional regime value of $V_{FG}(1e)$ by 2, and the value of $rV_{FG}(1e)$ by $\sqrt{2}$, well outside of the experimental uncertainty. Using $\Delta_\Phi = h/2e$, corresponding to excitation of one $e/5$ quasiparticle in the 2/5 island, yields $rV_{FG}(1e) = 3.26$ V·nm, implying 3.2 times weaker coupling of the island electrons to the front gates, whereas an approximately constant coupling is expected from the gate geometry. We thus conclude that values of $N_\Phi \leq 2.5$ are not consistent with the experimentally observed Δ_B and $d\Delta_B/dV_{FG}$.

Alternatively, without explicitly using N_Φ, we can rewrite the Eqs. 6.1−6.4 in terms of the outer ring area $S_{Out} = h/e\Delta_B$ from $f = 1$ and inner ring area S_{In} via the directly measured Δ_B and $d\Delta_B/dV_{FG}$. Requiring exact equality of the products $V_{FG}(1e)\sqrt{S_{In}}$ and $V_{FG}(1e)\sqrt{S_{Out}}$ obtained from the fractional

and the integer data, respectively, we obtain an equation for S_{In},

$$\sqrt{\frac{h}{e}}\frac{1}{B_1}\left[\frac{\sqrt{\Delta_B^3}}{d\Delta_B/dV_{FG}}\right]_{f=1} = \frac{h}{eB_1}\left[\frac{\Delta_B}{\sqrt{S_{In}}(d\Delta_B/dV_{FG})}\right]_{f=2/5}. \tag{6.5}$$

This gives

$$S_{In} = \frac{h}{e}\left[\frac{d\Delta_B/dV_{FG}}{\sqrt{\Delta_B^3}}\right]^2_{f=1} \times \left[\frac{\Delta_B}{d\Delta_B/dV_{FG}}\right]^2_{f=2/5}, \tag{6.6}$$

yielding $S_{In} = 0.92 \times 10^{-12}$ m^2 and $\Delta_\Phi = \Delta_B S_{In} = 2.0 \times 10^{-14}$ Wb$= 4.8h/e$ from the data of Figure 6.4, with an experimental uncertainty of $\pm 10\%$. The dominant source of experimental error is the uncertainty in the Δ_B versus V_{FG} slopes.

Although we do not use the electron density modeling in the data analysis presented above, it is interesting to compare the qualitative features of the front-gate bias dependence of the oscillatory data of the kind presented in Figure 6.4 to the calculated island electron density profile, Figure 6.2(b). The open and closed circles show the $n(r)$ positions obtained from the integer and the fractional Aharonov-Bohm data for $V_{FG} = 0$ and -300 mV, respectively. The fractional regime circles give radii using the flux period $\Delta_\Phi = 5h/e$. Only one of the four independent points is adjusted to fit the experiment, thus "calibrating" the depletion length parameter W. Both effects observed experimentally are consistent with the profile of Figure 6.2: the systematic shift of the same filling factor upon application of V_{FG}, and the systematic change of the Aharonov-Bohm oscillation period. It is also worth mentioning that a stable edge ring requires steep enough gradient of the confining potential, that is, steep $-e(\partial n/\partial r)$. The experimental fact that the fractional quantum Hall regime Aharonov-Bohm oscillations persist even upon application of a moderate $V_{FG} = -300$ mV rules out inner edge ring radii well inside the island, where the confining potential gradient is very small at $V_{FG} = 0$, so that application of a moderate negative V_{FG} would shrink the AB orbit to zero.

In conclusion, we report experiments on electron interferometer devices in the quantum Hall regime, focusing on determination of the Aharonov-Bohm magnetic field period $\Delta_B(V_{FG} = 0)$ and its front-gate voltage slope $d\Delta_B/dV_{FG}$ for electrons ($f = 1$) and for Laughlin quasiparticles (2/5 embedded in 1/3). The Aharonov-Bohm period and its derivative can be combined to give the increment of the gate voltage attracting charge $1e$, that is, the electrostatic coupling of electrons to the front gates, assuming the area of the AB orbit is known. This allows us to determine the fractional quantum Hall regime flux

period Δ_Φ directly, without reference either to a calculated electron density profile, or the tunneling distance consistent with the experimental amplitude of conductance oscillations. We find the fractional flux period $\Delta_\Phi = 5h/e$ is consistent, while $\Delta_\Phi \leq 2.5h/e$ are inconsistent with the front-gate bias experimental results.

6.2 Temperature dependence of the Aharonov-Bohm superperiod[2]

We measure the superperiodic oscillations at various temperatures for the interferometer sample and find the oscillations persist up to 140 mK, which is only an order of magnitude less than the $f = 2/5$ QH gap [62] and much larger than the quasiparticle quantization energy of the island-circling states. The high temperature dependence of the oscillation amplitude fits well the quantum-coherent thermal dephasing of an interference signal, with the activation energy ∼27 mK. These results are qualitatively different than that observed in quantum dot [63, 64], quantum antidot [28, 35, 65], and Coulomb blockade devices [66]. Therefore, the observed temperature data are probably resulted from the topological protection of the anyonic statistical interactions.

We studied sample M97Bm, with the detailed sample parameters introduced before. The four-terminal magnetoresistance is measured by passing a $I_X = 93$ pA rms ac current at 5.4 Hz and detecting the resulting voltage signal at the other two contacts by a lock-in technique. On the $f = 1/3$ QH plateau, the Hall voltage is $V_H = I_X(3h/e^2) \approx 7.2$ μV. Taking into account the additional "electromagnetic noise environment" on the sample [28, 65] yields a total voltage $\sqrt{7.2^2 + 2^2} = 7.5$ μV. The peak tunneling current that heats the island region is ∼0.8 pA, giving a heating power of $\sim 6 \times 10^{-18}$ W. The rest of the excitation and environmental noise is $\sim 7 \times 10^{-18}$ W, heating the relatively large Ohmic contacts immersed inside the ^{3}He−^{4}He mixture.

Superperiodic oscillations are observed in the FQH regime when the island filling is 2/5, embedded inside the 1/3 fluid, as described previously. Traces of the four-terminal resistance R_{XX} are obtained as a function of B for temperature range 10.2 mK $\leq T \leq$ 141 mK, see Figure 6.5. These oscillating data were obtained continuously over ∼70 h period following a ∼100 h sample stabilization time, demonstrating the stability of the superperiodic oscillations. The experimental data are analyzed as following. We determine the oscillation amplitudes for several regular oscillations as $\delta R_{XX}(T) = (R_{XX,MAX} - R_{XX,MIN})/2$

[2]Published in F.E. Camino, Wei Zhou, and V.J. Goldman, Phys. Rev. B **74**, 115301 (2006).

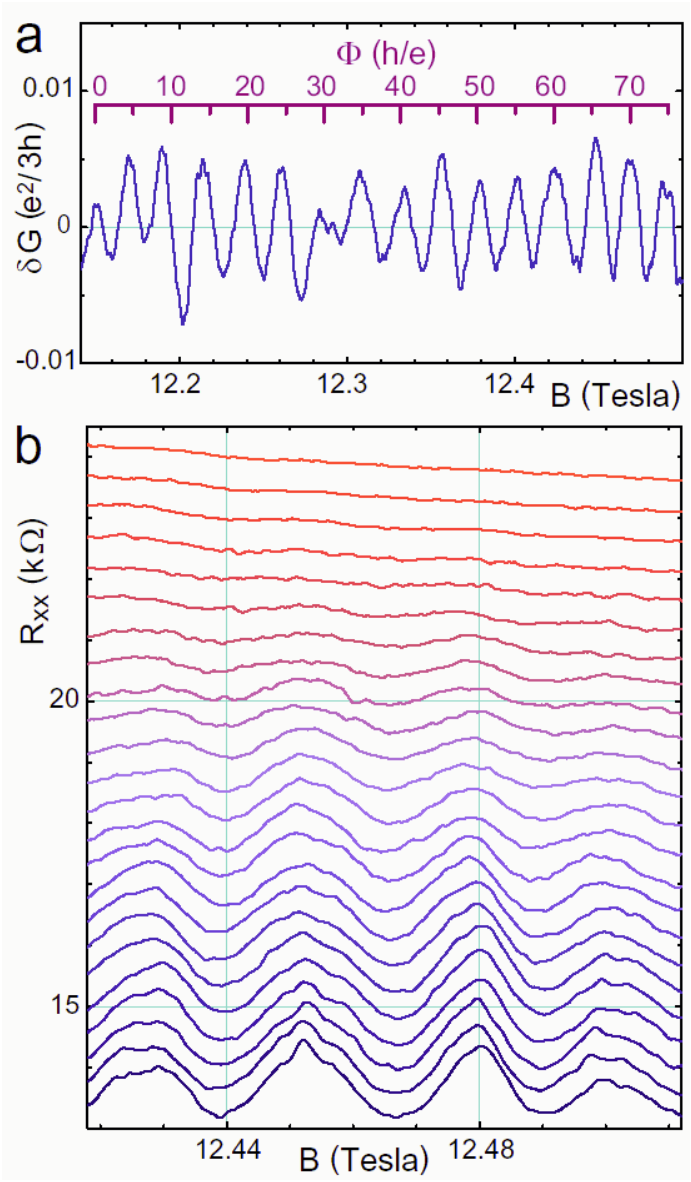

Figure 6.5: (a) Superperiodic oscillations observed when the $f = 2/5$ island is embedded in the $f = 1/3$ QH fluid. (b) Temperature dependence of the superperiodic oscillations. Each trace was taken at a different temperature from 10.2 mK (bottom trace) to 141 mK (top trace). The successive traces are vertically displaced by 0.4 kΩ. The data in (a) and (b) were obtained on different cooldowns of the sample.

for each trace. The oscillatory conductance δG is calculated from δR_{XX} and the quantized Hall resistance value $R_{XY} = 3h/e^2$ as $\delta G = \delta R_{XX}/(R_{XY}^2 - R_{XY}\delta R_{XX})$, which holds for $\delta R_{XX} \ll R_{XY}$ [28, 57, 65, 67]. Then δG is normalized against the average of the two lowest temperature values (10.2 mK and 11.9 mK), and the average of six thus determined values for each trace is used as δG for that specific temperature, in order to reduce the uncertainty. The normalized conductance amplitude $G_A(T)/G_A(11\text{mK})$ are shown in Figure 6.6 in linear and semi-log plots. It can be seen that the temperature varies by a factor of 14 and the normalized conductance varies by a factor of 31. From the semi-log plot of Figure 6.6(b), it is clear that the high-T behavior fits well to $\exp(-T/T_0)$, the expected dependence for thermal dephasing of a quantum-coherent interference signal, with $T_0 \approx 27$ mK.

The data for the interferometer sample are qualitatively different from that observed in the resonant tunneling experiments in quantum dots [63, 64] and antidots [28, 35, 65] or Coulomb blockade devices [66]. In resonant tunneling, a single tunneling peak is described by $G(X,T) = G_0/T\cosh^2(X/T)$, where X is the resonant tuning parameter [28]. The single peak conductance $G_P \propto 1/T$ [35]. For the Coulomb blockade case, which is not expected for the current device due to the wide constrictions, a single tunneling peak is given by $G(X,T) = G_0 X/T\sinh(X/T)$. The maximum conductance $G_{MAX}(T) \approx$ *const* because the single charge tunneling can proceed via many levels within a range $\propto T$, canceling the $1/T$ fermi-liquid prefactor. In the interferometer device, the activation $T_0 \approx 27$ mK while the oscillations are observable up to ∼140 mK. In contrast, for quantum antidot in the FQH regime [28, 65], the corresponding $T_0 \approx 120$ mK, and the oscillations are observable up to ∼80 mK. In the quantum dots [63, 64] and antidots [35] in the IQH regime, oscillations are observable up to $\sim 0.5T_0$.

Without taking account in the topological order of the two FQH condensates, one would imagine the flux period changes to $\Delta_\Phi = h/e$ at high temperatures. Thus, the observed thermal dephasing behavior and the fact that the Aharonov-Bohm superperiodic oscillations persist up to 140 mK suggests topological protection of the anyonic statistical interactions, which also demonstrates the stability of the superperiodic oscillations.

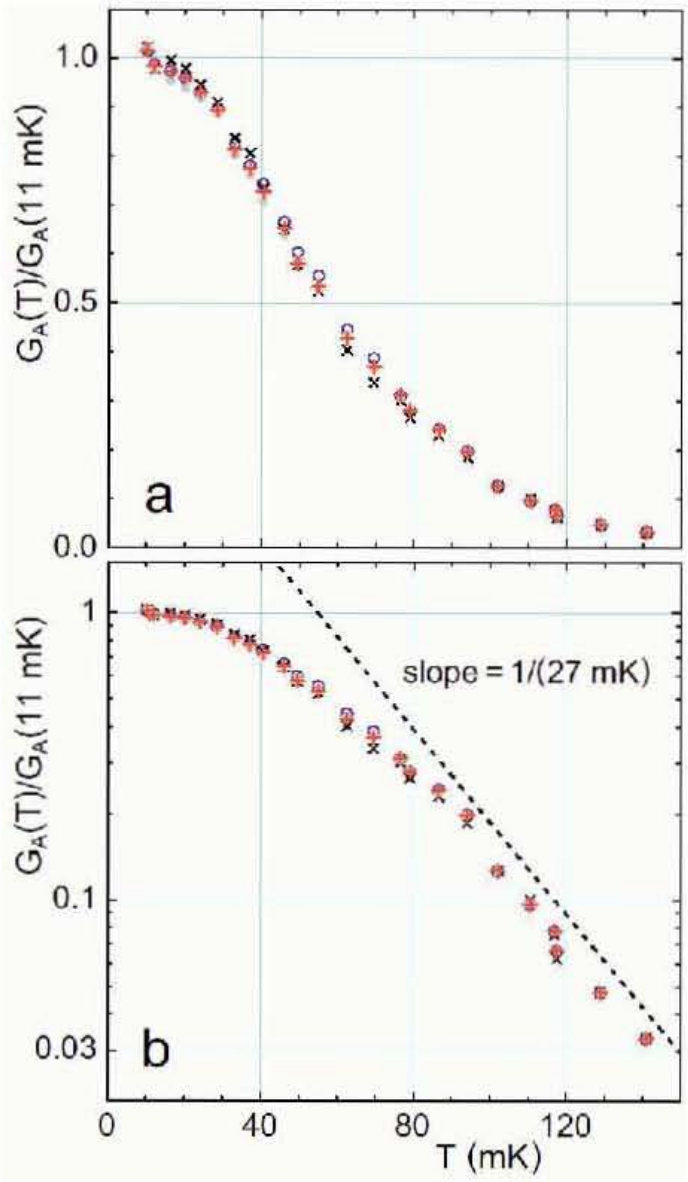

Figure 6.6: Temperature dependence of the normalized conductance oscillation amplitudes shown on linear and semi-log scale. The spread of data points illustrates the uncertainty.

Chapter 7

Conclusion

We designed and fabricated two kinds of novel Laughlin quasiparticle interferometer samples and performed measurements on them in the QH regime. The central interference region of the interferometer consists of an electron island defined by four etch trenches. The electron island is connected to the 2D bulk area by two nearly open constrictions. In the QH regime, counterpropagating edge channels are coupled by coherent tunneling in the constrictions, resulting a closed interference path around the electron island.

Aharonov-Bohm type conductance oscillations were observed both in the integer and fractional QH regime. In the IQH regime, the underlying particles are electrons of charge $-e$ and Fermi statistics. Therefore we calibrated the interferometer devices using the IQH regime data. For the $e/3$ primary-filling interferometer sample, we realized a regime where an island of $f = 1/3$ is enclosed by $f = 1/3$ edge channels. We obtained flux period $\Delta_\Phi = h/e$ and charge period $\Delta_Q = e/3$. From these results, statistics of the $e/3$ Laughlin quasiparticles can be directly calculated to be $\Theta_{1/3} = 2/3$, in agreement with theory predictions. For another kind of sample, where in the FQH regime an island of f =2/5 is embedded in the 1/3 fluid, we obtained $5h/e$ magnetic flux and $2e$ charge periods. To the best of our knowledge, flux period more than h/e has never been reported in an Aharonov-Bohm type interference experiments. The $5h/e$ Aharonov-Bohm superperiod directly demonstrates the anyonic nature of Laughlin quasiparticles.

We also studied the front-gate voltage dependence of the Aharonov-Bohm oscillations. Analysis of the results obtained from integer and fractional QH regimes provides an independent way to determine the flux period of the superperiodic oscillations. The flux period of $5h/e$ fits the data best. We also measured temperature dependence of the Aharonov-Bohm superperiodic oscillations. The oscillations persist to temperature $\sim$140 mK, which is only an order of magnitude less than the 2/5 QH gap. These data show the stable-

ness of the Aharonov-Bohm superperiods against moderate front-gate voltage changes and temperature variations.

In summary, we realized two kinds of novel Laughlin quasiparticle interferometers. Both the observed flux and charge periods are robust. These data clearly demonstrate the fractional statistics of Laughlin quasiparticles.

Bibliography

[1] K. von Klitzing, G. Dorda, and M. Pepper, Phys. Rev. Lett. **45**, 494 (1980).

[2] D. C. Tsui, H. L. Stormer, and A. C. Gossard, Phys. Rev. Lett. **48**, 1559 (1982).

[3] R. B. Laughlin, Phys. Rev. Lett. **50**, 1395 (1983).

[4] V. J. Goldman and B. Su, Science **267**, 1010 (1995); Physica E (Amsterdam) **1** 15, (1997).

[5] F. Wilczek, Phys. Rev. Lett. **48**, 1144 (1982); *ibid.* **49**, 957 (1982).

[6] B. I. Halperin, Phys. Rev. Lett. **52**, 1583 (1984).

[7] J. M. Leinaas and J. Myrheim, Nuovo Cimento Soc. Ital. Fis. B **37**, 1 (1977).

[8] X. G. Wen, Phys. Rev. B **41**, 12838 (1990).

[9] A. Y. Kitaev, Ann. Phys. (N.Y.) **303**, 2 (2003).

[10] Y. Aharonov and D. Bohm, Phys. Rev. **115**, 485 (1959).

[11] *The Quantum Hall Effect*, 2nd Ed., edited by R. E. Prange and S. M. Girvin (Springer, NY, 1990).

[12] D. Yoshioka, *The Quantum Hall Effect* (Springer, 2002).

[13] R. B. Laughlin, Rev. Mod. Phys. **71**, 863 (1999).

[14] R. B. Laughlin, Phys. Rev. B **23**, 5632 (1981).

[15] R. L. Willett *et al.*, Phys. Rev. Lett. **59**, 1776 (1987).

[16] W. Pan *et al.*, Phys. Rev. Lett. **83**, 3530 (1999).

[17] F. D. M. Haldane and E. H. Rezayi, Phys. Rev. Lett. **54**, 237 (1985).

[18] F. D. M. Haldane, Phys. Rev. Lett. **51**, 605 (1983).

[19] B. I. Halperin, Phys. Rev. B **25**, 2185 (1982).

[20] X. G. Wen, Int. J. Mod. Phys. B **6**, 1711 (1992).

[21] R. Dingle, H. L. Stormer, A. C. Gossard, and W. Wiegmann, Appl. Phys. Lett. **33**, 665 (1978).

[22] J. Singh, *Physics of Semiconductors and Their Heterostructures* (McGraw-Hill, 1993).

[23] F. Stern and S. Das Sarma, Phys. Rev. B **30**, 840 (1984).

[24] M. Shayegan, V. J. Goldman, C. Jiang, T. Sajoto, and M. Santos, Appl. Phys. Lett. **52**, 1086 (1988)

[25] M. Shayegan, V. J. Goldman, M. Santos, T. Sajoto, L. Engel, and D. C. Tsui, Appl. Phys. Lett. **53**, 2080 (1988)

[26] T. Sajoto, Y. W. Suen, L. Engel, M. B. Santos, and M. Shayegan, Phys. Rev. B **41**, 8449 (1990).

[27] Wei Zhou, F. E. Camino, and V. J. Goldman, proceedings of LT24, AIP Conference Proceedings Vol. **850**, 1351 (2006).

[28] I. J. Maasilta and V. J. Goldman, Phys. Rev. B **55**, 4081 (1997).

[29] V. J. Goldman, I. Karakurt, J. Liu, and A. Zaslavsky, Phys. Rev. B **64**, 085319 (2001).

[30] V. J. Goldman, J. Korean Phys. Soc. **39**, 512 (2001).

[31] B. J. van Wees *et al.*, Phys. Rev. Lett. **62**, 2523 (1989).

[32] P. L. McEuen *et al.*, Phys. Rev. Lett. **66**, 1926 (1991).

[33] J. K. Wang and V. J. Goldman, Phys. Rev. Lett. **67**, 749 (1991)

[34] J. K. Wang and V. J. Goldman, Phys. Rev. B **45**, 13479 (1992).

[35] I. Karakurt, V. J. Goldman, J. Liu, and A. Zaslavsky, Phys. Rev. Lett. **87**, 146801 (2001).

[36] D. Arovas, J. R. Schrieffer, and F. Wilczek, Phys. Rev. Lett. **53**, 722 (1984).

[37] M. V. Berry, Proc. R. Soc. London, Ser. A **392**, 45 (1984).

[38] W. P. Su, Phys. Rev. B **34**, 1031 (1986).

[39] J. K. Jain, Phys. Rev. Lett. **63**, 199 (1989).

[40] J. K. Jain, Adv. Phys. **41**, 105 (1992).

[41] F. E. Camino, W. Zhou, and V. J. Goldman, Phys. Rev. B **72**, 075342 (2005).

[42] F. E. Camino, W. Zhou, and V. J. Goldman, Phys. Rev. B **72**, 155313 (2005).

[43] F. E. Camino, W. Zhou, and V. J. Goldman, Phys. Rev. Lett. **95**, 246802 (2005).

[44] F. E. Camino, W. Zhou, and V. J. Goldman, Phys. Rev. B **74**, 115301 (2006).

[45] F. E. Camino, W. Zhou, and V. J. Goldman, Phys. Rev. Lett. **98**, 076805 (2007).

[46] W. Zhou, F. E. Camino, and V. J. Goldman, Phys. Rev. B **73**, 245322 (2006).

[47] C. de C. Chamon, D. E. Freed, S. A. Kivelson, S. L. Sondhi, and X. G. Wen, Phys. Rev. B **55**, 2331 (1997).

[48] S. A. Kivelson and V. L. Pokrovsky, Phys. Rev. B **40**, 1373 (1989).

[49] S. Kivelson, Phys. Rev. Lett. **65**, 3369 (1990).

[50] V. J. Goldman, Phys. Rev. B **75**, 045334 (2007).

[51] C. N. Yang, Rev. Mod. Phys. **34**, 694 (1962).

[52] A. Cappelli *et. al.*, Phys. Rev. B **58**, 16291 (1998).

[53] E. V. Tsiper, Phys. Rev. Lett. **97**, 076802 (2006).

[54] Y. Gefen and D. J. Thouless, Phys. Rev. B **47**, 10423 (1993).

[55] N. Byers and C. N. Yang, Phys. Rev. Lett. **7**, 46 (1961).

[56] B. Y. Gelfand and B. I. Halperin, Phys. Rev. B **49**, 1862 (1994).

[57] R. J. Haug, A. H. MacDonald, P. Streda, and K. von Klitzing, Phys. Rev. Lett. **61**, 2797 (1988).

[58] A. Auerbach, Phys. Rev. Lett. **80**, 817 (1998).

[59] J. K. Jain, S. A. Kivelson, and D. J. Thouless, Phys. Rev. Lett. **71**, 3003 (1993).

[60] S. Das Sarma, M. Freedman, and C. Nayak, Phys. Rev. Lett. **94**, 166802 (2005).

[61] P. Bonderson, A. Kitaev, and K. Shtengel, Phys. Rev. Lett. **96**, 016803 (2006).

[62] R. R. Du, H. L. Stormer, D. C. Tsui, L. N. Pfeiffer, and K. W. West, Phys. Rev. Lett. **70**, 2944 (1993).

[63] L. P. Kouwenhoven, D. G. Austing, and S. Tarucha, Rep. Prog. Phys. **64**, 701 (2001).

[64] C. W. J. Beenakker, Phys. Rev. B **44**, 1646 (1991).

[65] I. J. Maasilta and V. J. Goldman, Phys. Rev. B **57**, R4273 (1998).

[66] D. V. Averin and K. K. Likharev, in *Mesoscopic Phenomena in Solids* (Elsevier, Amsterdam, 1991), pp. 173−271.

[67] S. Washburn, A. B. Fowler, H. Schmid, and D. Kern, Phys. Rev. Lett. **61**, 2801 (1988).